An edited version of this paper was published by AGU. Copyright (2012) American Geophysical Union. Citation: Oshchepkov, S., et al. (2012), Effects of atmospheric light scattering on spectroscopic observations of greenhouse gases from space: Validation of PPDF-based $CO_2$ retrievals from GOSAT, J. Geophys. Res., 117, D12305, doi:10.1029/2012JD017505.

# Effects of atmospheric light scattering on spectroscopic observations of greenhouse gases from space: Validation of PPDF-based $CO_2$ retrievals from GOSAT

Sergey Oshchepkov,[1] Andrey Bril,[1] Tatsuya Yokota,[1] Isamu Morino,[1] Yukio Yoshida,[1] Tsuneo Matsunaga,[1] Dmitry Belikov,[1] Debra Wunch,[2] Paul Wennberg,[2] Geoffrey Toon,[3] Christopher O'Dell,[4] André Butz,[5] Sandrine Guerlet,[6] Austin Cogan,[7] Hartmut Boesch,[7] Nawo Eguchi,[8] Nicholas Deutscher,[9,10] David Griffith,[9] Ronald Macatangay,[9] Justus Notholt,[10] Ralf Sussmann,[11] Markus Rettinger,[11] Vanessa Sherlock,[12] John Robinson,[12] Esko Kyrö,[13] Pauli Heikkinen,[13] Dietrich G. Feist,[14] Tomoo Nagahama,[15] Nikolay Kadygrov,[16] Shamil Maksyutov,[1] Osamu Uchino,[1] and Hiroshi Watanabe[1]

Received 21 January 2012; revised 2 April 2012; accepted 13 May 2012; published 23 June 2012.

[1] This report describes a validation study of Greenhouse gases Observing Satellite (GOSAT) data processing using ground-based measurements of the Total Carbon Column Observing Network (TCCON) as reference data for column-averaged dry air mole fractions of atmospheric carbon dioxide ($X_{CO2}$). We applied the photon path length probability density function method to validate $X_{CO2}$ retrievals from GOSAT data obtained during 22 months starting from June 2009. This method permitted direct evaluation of optical path modifications due to atmospheric light scattering that would have a negligible impact on ground-based TCCON measurements but could significantly affect gas retrievals when observing reflected sunlight from space. Our results reveal effects of optical path lengthening over Northern Hemispheric stations, essentially from May–September of each year, and of optical path shortening for sun-glint observations in tropical regions. These effects are supported by seasonal trends in aerosol optical depth derived from an offline three-dimensional aerosol transport model and by cirrus optical depth derived from space-based measurements of the Cloud-Aerosol Lidar with Orthogonal Polarization (CALIOP) instrument. Removal of observations that were highly contaminated by aerosol and cloud from the GOSAT data set resulted in acceptable agreement in the seasonal variability of $X_{CO2}$ over each station as compared with TCCON measurements. Statistical comparisons between GOSAT and TCCON coincident measurements of $CO_2$ column abundance show a correlation coefficient of 0.85, standard deviation of 1.80 ppm, and a sub-ppm negative bias of $-0.43$ ppm for all TCCON stations. Global distributions of monthly mean retrieved $X_{CO2}$ with a spatial resolution of 2.5° latitude × 2.5° longitude show agreement within ~2.5 ppm with those predicted by the atmospheric tracer transport model.

[1]National Institute for Environmental Studies, Tsukuba, Japan.
[2]Division of Geological and Planetary Sciences, California Institute of Technology, Pasadena, California, USA.
[3]Jet Propulsion Laboratory, California Institute of Technology, Pasadena, California, USA.
[4]Department of Atmospheric Science, Colorado State University, Fort Collins, Colorado, USA.
[5]IMK-ASF, Karlsruhe Institute of Technology, Karlsruhe, Germany.
[6]Netherlands Institute for Space Research, Utrecht, Netherlands.
[7]Earth Observation Science, Space Research Centre, University of Leicester, Leicester, UK.
[8]Research Institute for Applied Mechanics, Kyushu University, Kyushu, Japan.
[9]School of Chemistry and Centre for Atmospheric Chemistry, University of Wollongong, Wollongong, New South Wales, Australia.
[10]Institute of Environmental Physics, University of Bremen, Bremen, Germany.
[11]IMK-IFU, Karlsruhe Institute of Technology, Garmisch-Partenkirchen, Germany.
[12]National Institute of Water and Atmospheric Research, Wellington, New Zealand.
[13]FMI-Arctic Research Center, Sodankylä, Finland.
[14]Max Planck Institute for Biogeochemistry, Jena, Germany.
[15]Solar-Terrestrial Environment Laboratory, Nagoya University, Nagoya, Japan.
[16]Laboratoire des Sciences du Climat et de l'Environnement, CEA, CNRS, UVSQ, IPSL, Gif-sur-Yvette, France.

Corresponding author: S. Oshchepkov, National Institute for Environmental Studies, 16-2 Onogawa, Tsukuba, Ibaraki 305-8506, Japan. (sergey.oshchepkov@nies.go.jp)


0148-0227/12/2012JD017505

**Citation:** Oshchepkov, S., et al. (2012), Effects of atmospheric light scattering on spectroscopic observations of greenhouse gases from space: Validation of PPDF-based $CO_2$ retrievals from GOSAT, *J. Geophys. Res.*, *117*, D12305, doi:10.1029/2012JD017505.

## 1. Introduction

[2] Atmospheric carbon dioxide ($CO_2$) is acknowledged as being the dominant anthropogenic greenhouse gas and an important factor in global climate change. Over the past century, the $CO_2$ concentration has significantly increased from about 280 ppm to 380 ppm ($\mu$mol/mol) due to the burning of fossil fuels as well as changes in land use and forestry associated with expanding human activities [*Intergovernmental Panel on Climate Change*, 2007]. Recent advances in carbon cycle science have heightened the need for accurate space-based global observations of $CO_2$ for use in quantifying surface fluxes of greenhouse gases [*Chevallier et al.*, 2007].

[3] The Greenhouse Gases Observing Satellite (GOSAT) was launched on 23 January 2009 to monitor the global distributions of greenhouse gases ($CO_2$ and $CH_4$) from space. The satellite has a Sun-synchronous orbit at an altitude of 666 km and a 3-day recurrence with the descending node around 13:00 local time. Over the 3-day orbital repeat cycle, GOSAT measures several tens of thousands of single soundings that cover the globe. The most useful observations for retrieving gas concentrations are limited to areas under clear-sky conditions; only about 10% of the total daytime satellite soundings are available for gas retrievals throughout the entire atmosphere. At the same time, the number of remaining data points collected by GOSAT far surpasses the current number of ground monitoring stations (approximately 200) registered in the World Data Centre for Greenhouse Gases (WDCGG) [*World Data Centre for Greenhouse Gases*, 2011]. GOSAT thus helps to fill gaps in the ground-based observation network and has shown promise for improved $CO_2$ surface flux inverse modeling [*Chevallier et al.*, 2009], even though the precision of individual soundings is less than that of observations by ground monitoring stations. Generally, a precision of $\sim$1.5 ppm or better for monthly mean column-averaged dry air mole fraction of $CO_2$ ($X_{CO2}$) on a regional scale with sub-ppm biases is required to improve estimates of surface $CO_2$ fluxes from those based on in situ measurements [e.g., *Rayner and O'Brien*, 2001; *Chevallier et al.*, 2009; *Kadygrov et al.*, 2009].

[4] Although space-based observations of greenhouse gases are usually processed under clear-sky conditions, atmospheric light scattering, such as from high-altitude subvisible cirrus or aerosols, is always present and can introduce large biases in retrieved gas amounts [*O'Brien and Rayner*, 2002; *Dufour and Bréon*, 2003; *Mao and Kawa*, 2004; *Aben et al.*, 2007; *Oshchepkov et al.*, 2008, 2009, 2011; *Reuter et al.*, 2010]. The primary source of these biases is the uncertainty in the modification of the light path through the atmosphere [*Oshchepkov et al.*, 2011].

[5] Several algorithms have been developed for processing spectroscopic observations of greenhouse gases from space. Most of the algorithms that have been developed include the numerical solution of the radiative transfer equation when modeling measured radiance spectra [*Bösch et al.*, 2006; *Connor et al.*, 2008; *Butz et al.*, 2009; *Reuter et al.*, 2010; *O'Dell et al.*, 2012; *Yoshida et al.*, 2011]. These are often referred to as full physics algorithms. The effects of atmospheric light scattering are taken into account using modeled vertical profiles of aerosol and cloud optical depth. Whether the vertical profiles of a set aerosol and cloud optical characteristics are assumed [*Yoshida et al.*, 2011] or retrieved [*O'Dell et al.*, 2012] simultaneously with gas amounts is a basic distinguishing feature of different versions of full physics algorithms. It is important to note that aerosol and cloud optical characteristics are very smooth spectral functions within the gas absorption bands and only optical path modification is essential for radiative transfer spectral calculations. Any other impacts of atmospheric light scattering on measured radiance spectra, such as those related to near-ground aerosols, can be taken into account by spectral polynomials of low orders when applying differential optical absorption spectroscopy (DOAS) [*Buchwitz et al.*, 2000; *Frankenberg et al.*, 2005].

[6] Another physical background to consider in regard to atmospheric light scattering is light path modification, which can be examined using the photon path length statistical characteristics and the equivalence theorem [*Bennartz and Preusker*, 2006]. This formalism has been used to develop the photon path length probability density function (PPDF) method [*Bril et al.*, 2007; *Oshchepkov et al.*, 2008, 2009] to rapidly process spectroscopic observations of greenhouse gases from space. The PPDF-based method is constructed to allow reduction to DOAS when neglecting light path modifications. It can also account for any a priori data on aerosol and cloud optical characteristics available in full physics algorithms [*Oshchepkov et al.*, 2009].

[7] These algorithms are currently under development using the experience gained from processing of actual GOSAT data. It is important to evaluate algorithms for satellite data processing, such as by validating their $CO_2$ retrievals using ground-based high-resolution Fourier Transform Spectrometer (FTS) observations from the Total Carbon Column Observing Network (TCCON) [*Wunch et al.*, 2011a]. *Morino et al.* [2011] compared data products retrieved operationally with the version 01.XX algorithm of the National Institute for Environmental Studies (NIES) with reference TCCON data, and found a large $X_{CO2}$ negative bias of $\sim$9 ppm. *Butz et al.* [2011] validated about 1 year of GOSAT data processing with the "RemoTeC" algorithm developed at the Netherlands Institute for Space Research (SRON) and the Karlsruhe Institute of Technology (KIT). They implemented the empirical correction of positive bias in surface pressure retrieval that permitted correction of the $X_{CO2}$ negative bias. *Wunch et al.* [2011b] evaluated version B2.8 and partially evaluated version B2.9 of the algorithm that is operationally used to process the GOSAT radiance spectra in the National Aeronautics and Space Administration (NASA) Atmospheric $CO_2$ Observations from Space (ACOS) project. In their study, the global negative bias seen in version B2.8 was adjusted according to the discrepancy between TCCON and space-based retrievals

of $X_{CO2}$ over Southern Hemisphere stations where the $X_{CO2}$ gradients were assumed to be small [*Wunch et al.*, 2011b]. The version B2.9 results had an empirical correction applied to the oxygen A-band spectroscopy, similar to the *Butz et al.* [2011] correction, and required no further adjustments using the TCCON data.

[8] This paper validates PPDF-based GOSAT data processing by comparing the retrievals of column-averaged dry air mole fraction of $CO_2$ seasonally with FTS ground-based measurements at each TCCON station. We also compare global distributions of the retrievals by atmospheric transport modeling and analyze seasonal and spatial variability in light path modification over each TCCON site. We consider this latter issue to be important for the validation because atmospheric light scattering can influence satellite data, whereas it has little influence on ground-based FTS measurements that record direct solar light transmitted through the atmosphere. In most cases, light path modification offers a physical explanation of the discrepancy between satellite- and ground-based $CO_2$ retrievals.

[9] The paper is organized as follows. Section 2 briefly outlines the basic specifications of the GOSAT instrument and the PPDF-based $CO_2$ retrieval method. In section 3, we describe the reference data sources for the $CO_2$ column-averaged dry air mole fractions used to validate the retrievals (TCCON and atmospheric transport model). Section 4 defines coincidence criteria for GOSAT and TCCON data selection. Section 5 presents results of the validation study in terms of $CO_2$ seasonal variability over each TCCON site (section 5.1), a pairwise TCCON–GOSAT $X_{CO2}$ statistical comparison (section 5.2), and validation of the retrieved $X_{CO2}$ global distribution (section 5.3) using atmospheric transport modeling. A summary and concluding remarks are given in section 6.

## 2. GOSAT Instruments and Data Processing

[10] In this section, we briefly outline the basic specifications of the GOSAT instruments related to this study (e.g., spectral bands, observation modes, cloud screening) and focus on the GOSAT data processing by the PPDF-based method that retrieves both $CO_2$ column abundance ($X_{CO2}$) and optical path modification.

### 2.1. GOSAT Specifications

[11] The GOSAT project has been promoted jointly by the Japan Aerospace Exploration Agency (JAXA); NIES, Japan; and the Ministry of the Environment (MOE), Japan [*Hamazaki et al.*, 2005; *Yokota et al.*, 2009; *Kuze et al.*, 2009]. GOSAT was successfully launched on 23 January 2009 to monitor global $CO_2$ and $CH_4$ amounts. The satellite is in a Sun-synchronous orbit with an equator crossing time of about 13:00 local time and an inclination angle of 98°. GOSAT flies at an altitude of approximately 666 km, completes an orbit in about 100 min, and operates on a global basis with a 3-day repeat cycle.

[12] GOSAT is equipped with two instruments, the Thermal And Near-infrared Sensor for carbon Observation–Fourier Transform Spectrometer (TANSO-FTS) and the TANSO Cloud and Aerosol Imager (TANSO-CAI), which have been described in detail by *Kuze et al.* [2009].

[13] TANSO-CAI is an ancillary imager that observes the state of the atmosphere and the surface during daytime. The image data from CAI are used to determine the existence of cloud over an extended area that includes the FTS' field of view as described by *Ishida and Nakajima* [2009]. Radiance in the visible and near-infrared bands (380, 674, 870, and 1600 nm) would provide additional basic information on aerosol and cloud properties, but these retrieval algorithms remain under development. Currently, TANSO-CAI data are used for cloud prescreening (section 4) and for the cloud spatial coherence test [*Yoshida et al.*, 2011].

[14] TANSO-FTS is the key instrument for observing $CO_2$ and $CH_4$ amounts in the atmosphere. It observes solar light reflected from the Earth's surface in the Short Wavelength Infra-Red (SWIR) region and thermal radiation from the Earth's surface and atmosphere in the Thermal Infra-Red (TIR) region. TANSO-FTS measures raw interferograms that are then converted to radiance spectra (Level 1B; L1B data). This instrument has three narrow bands in the SWIR region (0.76, 1.6, and 2.0 $\mu$m as the center; also referred to as TANSO-FTS bands 1, 2, and 3, respectively) and one wide band in the TIR region (5.56–14.3 $\mu$m; TANSO-FTS band 4) at a high spectral resolution (interval) of about 0.2 $cm^{-1}$. The full width at half-maximum of the instrument line shape function is about 0.27 $cm^{-1}$, which clearly identifies the rovibrational absorption lines of $CO_2$ and $CH_4$ in the observed spectra [*Kuze et al.*, 2009; *Yoshida et al.*, 2011]. TANSO-FTS band 4 data were not used in this study.

[15] For the SWIR bands, the incident light is divided by a polarization beam splitter. It is then simultaneously recorded as two orthogonal polarization components, designated "P" and "S," whose polarization axes are aligned roughly along and perpendicular to the direction of spacecraft motion, respectively. The TANSO-FTS collects interferograms within an instantaneous, circular field of view with a 15.8-mrad diameter, yielding footprints that are approximately 10.5 km in diameter for nadir observations.

[16] The TANSO-FTS has a pointing mechanism that allows it to conduct off-nadir observations within pointing mirror driving angles of $\pm 35°$ in the cross-track direction and $\pm 20°$ in the along-track direction. Over ocean, the TANSO-FTS also observes the glint spot, the point of specular reflection at the water surface. The TANSO-FTS pointing mechanism includes several point cross-track scan modes, a sun-glint tracking mode, and a target mode. Between 4 April 2009 and 31 July 2010 the 5-point cross-track scan mode was utilized for routine science observations. This mode has been changed to the three-point cross-track scan mode for all subsequent routine science observations from 1 August 2010. It yields footprints separated by ~263 km cross-track and ~283 km along-track [*Watanabe et al.*, 2010]. In this mode, each footprint is sampled three times.

### 2.2. PPDF-Based Method

[17] In this section, we apply the version of the PPDF-based method that incorporates PPDF retrievals as a prescreening step to identify GOSAT soundings that are not distinctly affected by atmospheric light scattering. These clear sky soundings are recognized by low values of PPDF parameters from band 1 (the threshold is defined below) when the optical path modification is negligible in bands 2

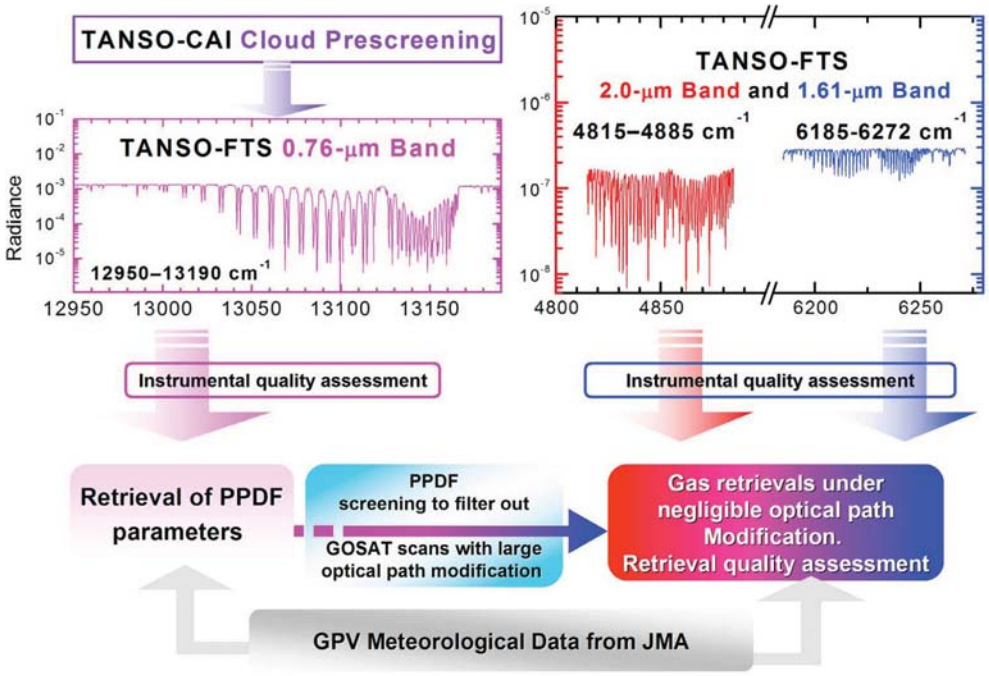


**Figure 1.** Simplified flowchart showing the basic steps for the PPDF-D level-2 data processing. PPDF parameters are retrieved in the oxygen A-band 1 (0.76 $\mu$m). GOSAT soundings with large light path modification are filtered out from further processing. The remaining GOSAT scans are used in the retrieval of $CO_2$ amounts at gas bands 2 (1.61 $\mu$m) and 3 (2.0 $\mu$m) with zero PPDF parameters.

and 3 [*Oshchepkov et al.*, 2011]. Then, we retrieve gas amounts from radiance spectra in bands 2 and 3 with PPDF parameters equal to zero, representing negligible optical path modification in these bands. This is shown to be equivalent to applying DOAS [*Oshchepkov et al.*, 2008]. We refer to this version as the NIES PPDF-D. Figure 1 presents a simplified flowchart of the data processing.

[18] Details of the PPDF-based method have been published elsewhere [*Bril et al.*, 2007; *Oshchepkov et al.*, 2008, 2009, 2011]. Below, we outline the key features of the PPDF-D inversion scheme and radiative transfer modeling.

[19] The GOSAT radiance spectra $R^*_{\Delta\nu j}$ ($\nu$: wave number, L1B data [*Kuze et al.*, 2009]) were processed with respect to retrievals of both PPDF parameters and gas amounts according to the maximum a posteriori rule:

$$\hat{\boldsymbol{x}} = \arg\min_{x}\left\{\left\|\boldsymbol{R}^* - \boldsymbol{R}'(\boldsymbol{x})\right\|^2_{C_R} + \left\|\boldsymbol{x}_a - \boldsymbol{x}\right\|^2_{C_a}\right\}. \qquad (1)$$

[20] In equation (1), $\boldsymbol{R}^*$ is the measurement vector ($\ln R^*_{\Delta\nu j}$), $\boldsymbol{R'}(\boldsymbol{x})$ is the vector of the radiative transfer forward model ($R'_{\Delta\nu j} = \ln\langle S^0_\nu \tilde{T}_\nu(\boldsymbol{x})\rangle_{\Delta\nu j} - P_{\Delta\nu j}$) at a set of spectral channels $\Delta\nu j$, $\boldsymbol{P}_{\Delta\nu j}$ is a spectral polynomial designed to remove the low-frequency portion of the processed spectra within each GOSAT band in the retrieval process (e.g., portions associated with near-ground aerosols or surface albedo), solar irradiance $S^0_\nu$ and the effective transmittance $\tilde{T}_\nu(\boldsymbol{x})$ spectra are convolved with the GOSAT instrumental line-shape function within each channel $\Delta\nu j$, $\boldsymbol{x}$ is a retrieval state vector with a priori $\boldsymbol{x}_a$, and the squared norms $\|\boldsymbol{z}\|^2_C = \boldsymbol{z}^{\mathrm{T}}\boldsymbol{C}^{-1}\boldsymbol{z}$ are weighted by covariance matrices of measurement errors of $\boldsymbol{R}^*$ ($\boldsymbol{C}_R$) and of a priori assumptions $\boldsymbol{x}_a$ ($\boldsymbol{C}_a$). PPDF parameters are spectrally identical (wavelength independent) over each GOSAT spectral band [*Bril et al.*, 2007; *Oshchepkov et al.*, 2008]. The effective transmittance and Jacobians are analytically expressed through either gas profiles or PPDF parameters allowing for rapid radiative transfer spectral calculations in the data processing.

[21] Under negligible light path modification, this method reduces to DOAS-based retrievals with a simplified expression for the effective transmittance at an altitude $h$ in equation (1):

$$\tilde{T}_\nu[x(h)] = \exp\left\{-\left(\frac{1}{\cos\Theta} + \frac{1}{\cos\Theta_0}\right)\tau_g\right\}, \qquad (2)$$

where $\tau_g = \int_0^{h_A} k_\nu(h)\,dh$ is the optical depth of gaseous atmosphere (in the vertical direction); $\Theta$ and $\Theta_0$ are the solar zenith angle and ray incident angle to the satellite, respectively; $k(h)$ is the vertical profile of the gas absorption coefficient; and $h_A$ is the top altitude of the absorbing atmosphere [*Oshchepkov et al.*, 2008]. Atmospheric light scattering could modify the optical path $\left(\frac{1}{\cos\Theta} + \frac{1}{\cos\Theta_0}\right)\tau_g$ through modification of the path length depending on aerosol and cloud optical properties, such as the aerosol and cloud optical depth, single scattering albedo, and scattering phase function within each individual atmospheric layer $\Delta h$.

[22] Two key PPDF parameters, $\alpha$ and $\rho$, are mainly responsible for the optical path modifications in the PPDF

model. They are retrieved in the oxygen A-band (12,950–13,190 $cm^{-1}$) and have the following physical interpretations:

[23] 1. Parameter $\alpha$ is the relative cloud/aerosol layer reflectivity, i.e., the ratio of photons scattered by the cloud/aerosol to the total number of photons within the field of view of the satellite detector (it is clear by definition that $\alpha$ increases as the surface albedo decreases);

[24] 2. Parameter $\rho$ is the scaled first moment of the PPDF under the cloud or within the aerosol layer, i.e., this parameter describes the path length modification due to multiple scattering/reflection between the ground surface and cloud/aerosol particles ($\rho$ increases with increasing surface albedo because of the higher probability that contributing photons will survive after multiple interactions with the surface).

[25] The admissible level of these parameters in the oxygen A-band within which the optical path modification due to aerosol and clouds is negligible in the gas absorption bands was set empirically at 0.04. These values are roughly appropriate for Rayleigh light scattering in the oxygen A-band of absorption at 0.76 $\mu$m [*Oshchepkov et al.*, 2011].

[26] The retrieved state vector in the $CO_2$ absorption bands at 1.61 $\mu$m (6368–6192 $cm^{-1}$) and at 2.0 $\mu$m (4815–4885 $cm^{-1}$) included a vertical profile of the $CO_2$ mixing ratio $\hat{x}_{CO2}(h)$ distributed over pre-defined pressure levels, and a scaling factor for water vapor the *prior* profile. The retrieved $CO_2$ profile was converted to $X_{CO2}$ at a given pressure increment using the following expression:

$$\hat{X}_{CO2} = \frac{1}{\int_0^{h_A} N_{dry} dh} \int_0^{h_A} N_{dry} \hat{x}_{CO2}(h)\, dh \qquad (3)$$

where $N_{dry}$ is the dry air number concentration.

[27] The stretch factor was included in the desired state vector in all bands for adjusting the position of the wave number grids to the observational spectra. Temperature and surface pressure were predefined and derived from Grid Point Value (GPV) data provided by the Japan Meteorological Agency (JMA). Constraints on the retrieved $CO_2$ profiles were unified: an altitude-independent 385-ppm a priori profile with a 30-ppm a priori standard deviation for all pressure levels and GOSAT soundings. For the assumed diagonal matrix $\boldsymbol{C_a}$ these constraints correspond to ~6–8 ppm uncertainty in $X_{CO2}$ depending on the surface pressure.

[28] We apply a unified retrieval scheme to processing the GOSAT observations over land and for both regular and sunglint observation modes over ocean using the "P" polarization state (section 2.1). A post-processing and instrumental quality assessment eliminated retrieved results for which the discrepancy between the forward model and the observed spectrum was significant (chi-square $\chi^2 > 5$, where $\chi^2$ is defined within the curly braces of equation (1)), signal-to-noise ratio (SNR) <75 for each spectral band, and degrees of freedom for the signal (DFS) ≤ 1 [*Rodgers*, 2000] to ensure the low impact of a priori assumptions on a posteriori $X_{CO2}$ estimations.

## 3. Ground-Based and Modeled $X_{CO2}$ Data

[29] This section briefly describes the sources of reference data for validating GOSAT $X_{CO2}$ retrievals. We focused on validation using TCCON ground-based FTS measurements. A NIES global atmospheric tracer transport model is used as an ancillary for three reasons: for selection of GOSAT observations when applying the confidence criteria (section 4), to fill gaps in seasonal variations of $X_{CO2}$ when TCCON data were not available (section 5.1), and as a part of the validation of $X_{CO2}$ retrievals on a global scale (section 5.3).

### 3.1. TCCON FTS Data

[30] The Total Carbon Column Observing Network was established in 2004 with a primary focus on measuring precise and accurate columns of $CO_2$, $CH_4$, and other atmospheric constituents. It is a ground-based network of high-resolution FTSs recording direct solar absorption spectra in the near-infrared spectral region. The scientific goals of the network are to improve our understanding of the carbon cycle, to provide a transfer standard between satellite measurements and ground-based in situ measurements, and to compile a primary validation data set for retrievals of $X_{CO2}$ and $X_{CH4}$ from space-based instruments, such as the Scanning Imaging Absorption Spectrometer for Atmospheric Cartography (SCIAMACHY), Tropospheric Emission Spectrometer (TES), Atmospheric Infrared Sounder (AIRS), Orbiting Carbon Observatory-2 (OCO-2) instrument, and TANSO-FTS [*Wunch et al.*, 2010, 2011a; *Morino et al.*, 2011].

[31] TCCON data processing uses the GFIT nonlinear least squares spectral fitting algorithm developed at NASA's Jet Propulsion Laboratory [*Toon*, 1992; *Wunch et al.*, 2011a]. The retrieved TCCON $X_{CO2}$ data are corrected for air mass-dependent artifacts [*Wunch et al.*, 2011a; *Deutscher et al.*, 2010]. Aircraft profiles measured over most of these stations were used to determine an empirical scaling factor to place the TCCON data on the World Meteorological Organization (WMO) standard reference scale. On average, the uncertainty in $X_{CO2}$ from the ground-based FTS measurement was estimated to be 0.8 ppm by comparing the TCCON retrievals with aircraft measurements [*Wunch et al.*, 2010; *Deutscher et al.*, 2010; *Messerschmidt et al.*, 2010]. Below, we use the uncertainties from individual TCCON and GOSAT soundings as weights when averaging $X_{CO2}$ data according to TCCON and GOSAT coincidence criteria (section 4).

[32] Figure 2 shows the locations of the TCCON stations from which the data analyzed in this study were obtained (yellow stars). Although the Moshiri site (red cross) is not included in the TCCON, the FTS at this station is operating under the TCCON observational protocol (IFS120HR). The spatial coordinates of these stations are listed Table 1.

### 3.2. NIES Transport Model

[33] Simulated $X_{CO2}$ values for GOSAT and TCCON observations were prepared with the NIES global atmospheric tracer transport model (NIES TM). NIES TM is an offline model driven by the Japanese 25-year Reanalysis (JRA-25) and JMA Climate Data Assimilation System (JCDAS) data covering more than 30 years from 1 January 1979 [*Onogi et al.*, 2007]. The present version (NIES-08.1i) of NIES TM uses a flexible hybrid sigma-isentropic ($\sigma$-$\theta$) vertical coordinate, which combines both terrain-following and isentropic levels switched smoothly near the tropopause. Vertical transport in the stratosphere is controlled by the climatological heating rate derived from JRA-25/JCDAS


**Figure 2.** Global locations of 12 ground-based FTS stations (yellow stars and red cross). Stars show 11 operational TCCON sites whose ground-based FTS data were used in this study. The site of future ground-based FTS measurements at Ascension Island (red star) was used to demonstrate the large impact of optical path modifications on GOSAT data processing due to atmospheric light scattering over the ocean. Although the Moshiri site (red cross) does not belong to TCCON, the FTS at this station is operating under the TCCON observational protocol.

reanalysis, which was adjusted to fit to the observed mean age of the air in the stratosphere.

[34] The model uses a flux-form advection algorithm with a second-order van Leer scheme and deep convection following *Tiedtke* [1989], with penetrative updraft mass fluxes adjusted to the JRA-25/JCDAS convective precipitation rate, a turbulent diffusion calculation as described by *Maksyutov et al.* [2008], and a bulk boundary layer with a 3-hourly planetary boundary layer height taken from the ERA-Interim reanalysis. Further details, except for the recently added hybrid sigma-isentropic coordinate option and implementation of JCDAS meteorological data, have been described elsewhere [*Belikov et al.*, 2011, 2012].

[35] NIES TM has been evaluated against GLOBALVIEW-$CO_2$ and WDCGG observations [*Belikov et al.*, 2011], through transport model intercomparison studies by *Niwa et al.* [2011] based on $CO_2$ data from the Comprehensive Observation Network for Trace Gases by Airliner (CONTRAIL) aircraft

**Table 1.** The Number of Available GOSAT Single Scans ($N_S$), Percentage of Remaining Scans After PPDF Screening ($R_{\%}$), Number of GOSAT Scans Coincident With TCCON Data ($N_C$), Number of Average Points ($N_a$) Meeting the Coincidence Criteria, and Characteristics of Statistical Relationships (5)–(8) Between Ground-Based FTS and GOSAT $X_{CO2}$ for Each TCCON Site

| TCCON Site: Global Location | $N_S$ | $R_{\%}$ (%) | $N_C$ | $N_a$[a] | $a \pm \sigma_a$ | Bias (ppm) | $\sigma_{GF}$ (ppm) | $r$ | $R^2$ |
|---|---|---|---|---|---|---|---|---|---|
| Sodankyla: 67.4°N, 26.6°E | 386 | 77 | 253 | 19 | 1.34 ± 0.13 | −1.69 | 2.29 | 0.90 | 0.84 |
| Bialystok: 53.2°N, 23.1°E | 1179 | 53 | 652 | 45 | 1.01 ± 0.05 | −0.07 | 1.25 | 0.95 | 0.91 |
| Bremen: 53.1°N, 8.85°E | 824 | 60 | 237 | 24 | 0.89 ± 0.09 | −1.87 | 2.74 | 0.77 | 0.62 |
| Orleans: 48.0°N, 2.11°E | 1183 | 61 | 432 | 37 | 0.83 ± 0.07 | −0.23 | 1.62 | 0.88 | 0.79 |
| Garmisch: 47.5°N, 11.1°E | 1502 | 59 | 1140 | 65 | 0.89 ± 0.05 | −0.43 | 1.41 | 0.90 | 0.84 |
| Park Falls: 45.9°N, 90.3°W | 2777 | 67 | 2289 | 68 | 1.19 ± 0.05 | −0.34 | 1.66 | 0.94 | 0.91 |
| Moshiri: 44.4°N, 142.3°E | 773 | 59 | 226 | 24 | 1.29 ± 0.17 | 0.38 | 2.84 | 0.82 | 0.96 |
| Lamont: 36.6°N, 97.5°W | 5299 | 76 | 5271 | 95 | 1.01 ± 0.05 | −0.56 | 1.20 | 0.92 | 0.90 |
| Tsukuba: 36.0°N, 140.2°E | 906 | 52 | 279 | 35 | 1.21 ± 0.12 | 0.04 | 1.50 | 0.91 | 0.97 |
| All northern TCCON sites | 14829 | 65 | 1079 | 412 | 1.02 ± 0.02 | −0.47 | 1.65 | 0.90 | 0.86 |
| Ascension Is.: 7.9°S, 14.3°W | 2603 | 27 | – | – | – | – | – | – | – |
| Darwin: 12.4°S, 130.9°E | 2114 | 36 | 871 | 38 | – | −1.76 | 1.36 | – | – |
| Wollongong: 34.4°S, 150.9°E | 2579 | 59 | 1717 | 64 | – | 0.86 | 1.44 | – | – |
| Lauder: 45.0°S, 169.7°E | 103 | 30 | 58 | 28 | – | −1.66 | 2.71 | – | – |
| All southern TCCON sites | 4796 | 45 | 2646 | 130 | – | −0.38 | 2.05 | – | – |
| All TCCON sites | 19625 | 59 | 1345 | 542 | 0.98 ± 0.02 | −0.43 | 1.80 | 0.85 | 0.78 |

[a]Both data sets were averaged weekly within 15°-latitude × 45°-longitude grid boxes centered at each TCCON station.

measurements, and by *Patra et al.* [2011] using $CH_4$ and $SF_6$ observations. NIES TM is able to reproduce the observed seasonal patterns of $CO_2$ in near-surface layers and in the free troposphere. Implementation of the hybrid sigma-isentropic vertical coordinate allows for simulation of seasonal mean vertical profiles and of the vertical propagation of seasonal variations in tracers in the troposphere and lower stratosphere that agree well with aircraft and balloon observations. In general, the performance of NIES TM is consistent with models participating in the TransCom intercomparison, although small biases in simulated interhemispherical gradients of $SF_6$ [*Patra et al.*, 2011] and $CO_2$ [*Niwa et al.*, 2011] were found.

[36] The model was run at a horizontal resolution of 2.5° × 2.5° and 32 vertical levels from the surface up to the level of 3 hPa. The $CO_2$ simulation for the period of 2000–2011 (we used 2000–2001 as a spin-up period) utilized the initial $CO_2$ global distribution derived from *GLOBALVIEW-$CO_2$* [2010] observations [*Belikov et al.*, 2012]. We use prescribed fluxes from the CONTRAIL model intercomparison [*Niwa et al.*, 2011], as follows:

[37] 1. Interannually varying anthropogenic emissions are derived from the Emission Database for Global Atmospheric Research (EDGAR-1998) with annual mean distribution [*Olivier and Berdowski*, 2001]. The emission totals are scaled using the growth rate of the top 20 country-specific fossil fuel consumptions from the Carbon Dioxide Information Analysis Center [*Boden et al.*, 2009];

[38] 2. Distribution of all natural (non-fossil) sources/sinks over land and ocean is represented by the inversion flux, derived by inverse modeling with 12 TransCom3 models [*Gurney et al.*, 2004] and observational data from GLOBALVIEW-$CO_2$ at 87 sites in the period of 1999–2001 [*Miyazaki et al.*, 2008].

[39] The 2007 fluxes were used from 2008 onwards.

## 4. GOSAT, TCCON, and NIES TM Data Selection

[40] We analyzed data from 22 months of GOSAT operation from June 2009 to March 2011. The analyzed observations fell into the category of cloud-free scenarios detected by TANSO-CAI [*Kuze et al.*, 2009] when applying the cloud flag test developed by *Ishida and Nakajima* [2009]. After eliminating cloudy observations, we had approximately 700,000 GOSAT single scans over both land and ocean. As *Nakajima et al.* [2008] noted, TANSO-CAI often fails to detect optically thin cirrus clouds because it has no thermal infrared channel that is sensitive to the presence of clouds in the upper troposphere. On the basis of actual data processing, *Yoshida et al.* [2011] also found that the TANSO-CAI cloud flag test tended to categorize subpixel-sized clouds as clear pixels over the ocean. Thus, the GOSAT observations in this data set may contain contamination by light scattering from thin cirrus clouds. We consider the effects of atmospheric light scattering by examining the retrieved optical path modification in the GOSAT validation study. The seasonal variability of PPDF parameters is supported with data from the Cloud Aerosol Lidar with Orthogonal Polarization (CALIOP) instrument onboard the Cloud-Aerosol Lidar and Infrared Pathfinder Satellite Observations (CALIPSO) platform [*Winker et al.*, 2007].

[41] The number of ground-based FTS and GOSAT coincident observations within spatially small pixels around TCCON stations is rather limited [*Morino et al.*, 2011]. Our TCCON–GOSAT coincidence criteria for validating the PPDF-based retrievals included weekly mean GOSAT data within 15°-latitude × 45°-longitude grid boxes centered at each TCCON station. For these grid boxes, we excluded GOSAT observations for which the global atmospheric tracer transport model (mod $X_{CO2}$) showed >1 ppm difference from modeled $X_{CO2}$ at the TCCON site (mod $X_{CO2}^{TCCON}$):

$$\left|\mathrm{mod}\,X_{CO2} - \mathrm{mod}\,X_{CO2}^{TCCON}\right| \le 1\,ppm. \quad (4)$$

[42] We chose this value to limit spatial and temporal variability in $X_{CO2}$ to within the a posteriori standard deviation of $X_{CO2}$ derived by PPDF-D retrievals (~0.8–2 ppm). A similar approach to extending the sample size was made by *Wunch et al.* [2011b] with a larger grid box size (30° latitude × 60° longitude) and longer period of 10 days, which included at least three GOSAT repeat cycles. They used potential temperature constraints (±2 K) at 700 hPa to minimize the variability in $X_{CO2}$, which is dynamic in origin [*Keppel-Aleks et al.*, 2011], when defining coincidence criteria in the Northern Hemisphere and used TCCON measurements in the Southern Hemisphere when defining the global $X_{CO2}$ bias. We limited the ground-based FTS data to ±1 h of the GOSAT overpass time. The same temporal limitation was used for sampling the NIES TM simulated concentration. The modeled $X_{CO2}$ data were taken from the spatial grid cell (with horizontal a resolution of 2.5° × 2.5°) containing the TCCON site. In this study, we use initial data when comparing $X_{CO2}$ from GOSAT, TCCON, and NIES TM without considering the averaging kernel effect.

## 5. Validation of PPDF-Based Retrievals

### 5.1. Seasonal Variations

#### 5.1.1. Northern Hemisphere Stations

[43] Figures 3 (left) and 4 (top) display 22-month seasonal variations in $X_{CO2}$ retrievals (blue symbols) in comparison with those derived by ground-based FTS measurements (green symbols). Six TCCON stations in the Northern Hemisphere (from north to south: Sodankyla, Bialystok, Garmisch, Park Falls, Lamont, and Tsukuba) were chosen (Figure 3, top to bottom, and Figure 4, top). As noted in section 4, all $X_{CO2}$ data were weekly means. For temporal correspondence, the ground-based FTS data were limited to ±1 h of the GOSAT overpass time. The GOSAT mean values $Y_i = \sigma_i^2(\mathbf{1}^T\mathbf{C}_i^{-1}\mathbf{Y}^i)$ and their variance $\sigma_i^2 = (\mathbf{1}^T\mathbf{C}_i^{-1}\mathbf{1})^{-1}$ were computed for noncorrelated noise of $k$ single scans within the coincidence criterion, where $\mathbf{1}$ and $\mathbf{Y}^i$ are $k$ dimensional vector-columns of unity and $X_{CO2}$, respectively, and $\mathbf{C}_i$ is the $k \times k$ diagonal covariance matrix of $\mathbf{Y}^i$. TCCON data were processed in the same way. Bars in Figure 3 display the standard deviations (± $1\sigma_i$) for both GOSAT and TCCON $X_{CO2}$. In Figures 3 and 4, we also plot the $X_{CO2}$ time series according to NIES TM (red crosses) for the GOSAT soundings that were available for PPDF-based data processing after the quality assessment (section 2.2). Observations over both land and ocean were included in the comparison if the GOSAT scans satisfied the coincidence criteria in equation (4).

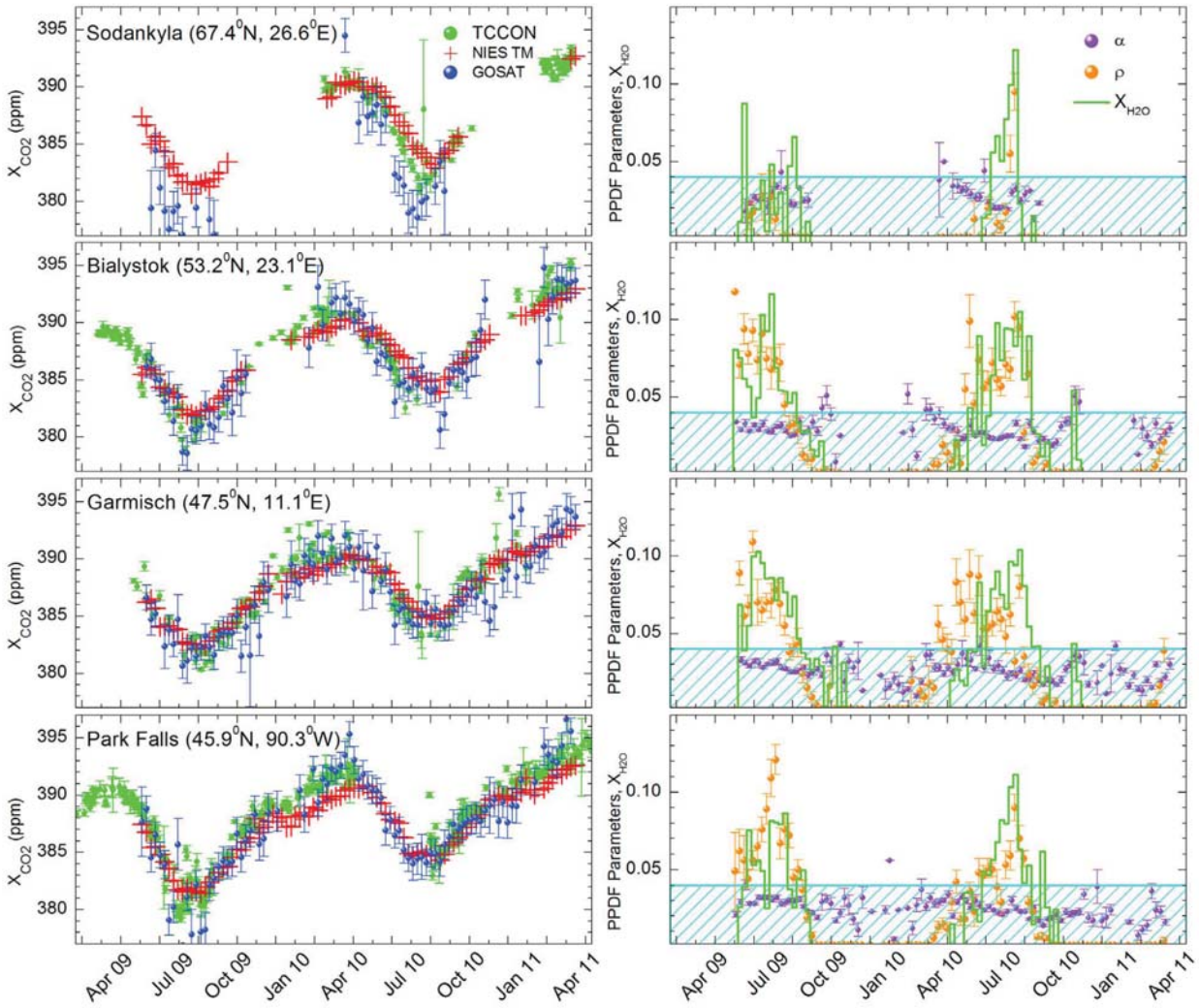


**Figure 3.** (left) Time series of $X_{CO2}$ and (right) PPDF parameters and average water vapor column abundance $X_{H2O}$ obtained from meteorological data of JMA over four TCCON stations (the station name is given in the left panels) in the Northern Hemisphere within 15°- latitude × 45°-longitude grid boxes centered at each TCCON station. For clearer display within the same axis scale, $X_{H2O}$ (mole fractions) was multiplied by a factor of 30. The number of available GOSAT single scans for each TCCON station is listed in Table 1 ($N_S$). The light blue shaded areas in the right panels represent the 0.04 threshold beyond which the retrievals were eliminated.

[44] For each TCCON station, Figures 3 (right) and 4 (middle) show time series of PPDF parameters ($\alpha$ blue and $\rho$ orange symbols) and water vapor column abundance ($X_{H2O}$, green histograms). The $X_{H2O}$ data were calculated from a priori water vapor profiles provided by the JMA.

[45] Most retrieved values of $\alpha$ were within the threshold of 0.04 (except over Tsukuba), and no remarkable seasonal trend was found for the shortening of the light path (blue symbols in Figure 3 (right) are within the filled area). We explain this by the very limited number of glint observations in the Northern Hemisphere around these stations, where dark surfaces could cause significant shortening of the optical path (section 5.1.2). At the same time, the effects of light path lengthening are clearly discernible in the increased values of $\rho$ from May–September each year (orange symbols in Figure 3, right). The similar seasonal trends in water vapor column abundance shown by green histograms in Figure 3 (right) provide supporting circumstantial evidence for the path length modifications due to light scattering by aerosols or clouds.

[46] Removal of contaminated observations ($\alpha$ and $\rho > 0.04$) from the GOSAT data set results in acceptable agreement between the seasonal variability of $CO_2$ at each station and the TCCON measurements (Figure 3, left). Overall, PPDF-D $X_{CO2}$ retrievals reproduce the temporal and spatial patterns observed in the TCCON measurements and simulated by NIES TM well. The disagreement between GOSAT and ground-based FTS $X_{CO2}$ is mostly within the error bars of satellite-based $X_{CO2}$ data. A clear and

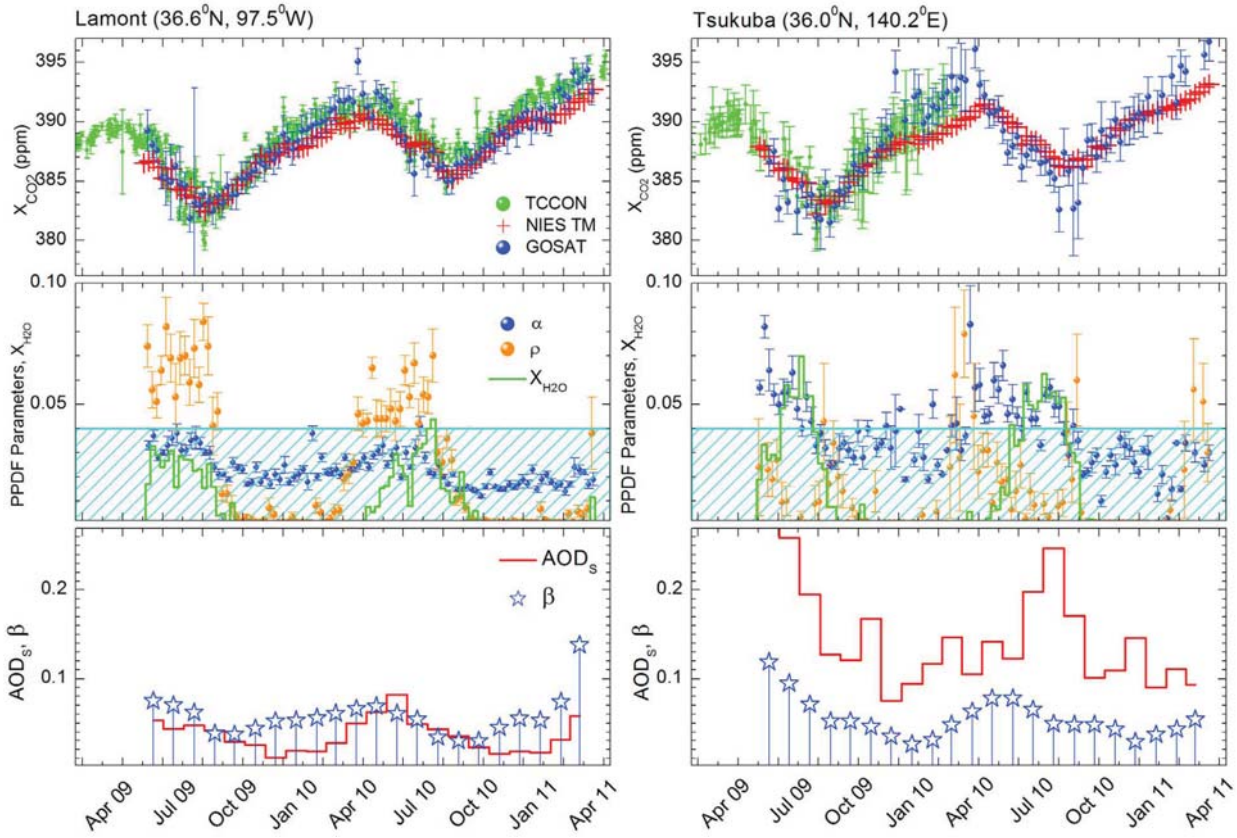


**Figure 4.** Validation of GOSAT retrievals and characteristics of atmospheric light scattering (left) over Lamont and (right) over Tsukuba. (top) Time series of $X_{CO2}$ from TCCON (green symbols), GOSAT (blue symbols), and NIES TM (red crosses). (middle) Time series of PPDF parameters $\alpha$ (blue symbols), $\rho$ (orange symbols), and average water vapor column abundance $X_{H2O}$ (green histogram). For clearer display within the same axis scale, $X_{H2O}$ [mole fractions] was multiplied by a factor of 10. (bottom) Time series of aerosol optical depth (AOD) from the SPRINTARS model (red histogram) and from the product of the cirrus fraction by cirrus optical depth ($\beta$, stars) derived from CALIOP data.

pronounced seasonal cycle of $CO_2$ column abundance can be seen, with minimums in late summer and maxima in spring. The largest amplitude of the seasonal trend was found at Park Falls, as previously reported in the GOSAT validation study by *Butz et al.* [2011]. This large amplitude may be attributable to the large forest area surrounding Park Falls, which is known to be a strong sink of $CO_2$ in summer, as well as to increased fossil fuel consumption in the winter season.

[47] Retrievals over Sodankyla demonstrate the limits of GOSAT SWIR observations at high latitudes, even on a seasonal time scale (Figure 3, top), due to large solar zenith angles, cloudy conditions, and ice-covered surfaces.

[48] We present $X_{CO2}$ validation results over Lamont and Tsukuba in Figure 4. These stations are located at almost the same latitude of ~36°N but the surrounding areas have different effects of atmospheric light scattering, as well as different surface properties. Figure 4 (bottom) shows the seasonal variability in aerosol optical depth (AOD - red histogram) at the 1.6-$\mu$m wavelength calculated from an offline three-dimensional aerosol transport model, the Spectral Radiation-Transport Model for Aerosol Species (SPRINTARS) [*Takemura et al.*, 2000]. This panel also shows the product of the cirrus fraction by cirrus optical depth at the 532-nm wavelength ($\beta$ - blue stars) derived from observations by CALIOP, which is the primary instrument carried by CALIPSO [*Winker et al.*, 2007]. Here and in the following sections, the SPRINTARS (AOD) and CALIOP ($\beta$) data have a spatial resolution of 2.8°-latitude × 2.8°-longitude and 5°-latitude × 5°-longitude grid boxes. Whereas the seasonal trends and magnitude of cirrus optical prosperities are similar for both stations (blue stars in Figure 4, bottom), the values of AOD (red histograms) are significantly larger over the Tsukuba site. This could be attributable to light scattering by windborne soil and mineral dust aerosols, which are transported to Japan from the Gobi and Takla Makan deserts in China due to sandstorms [*Shimizu et al.*, 2004]. Global distributions of the aerosol optical depth from SPRINTARS in Figure 5 (top) support this idea; the dark green area (indicating large AOD) covers Japan in July (Figure 5, left). Tsukuba is near Kasumigaura Lake and 57 km west of the Pacific Ocean. A large amount of elevated aerosols and subvisible cirrus over the dark surface around this station lead to the shortening of the

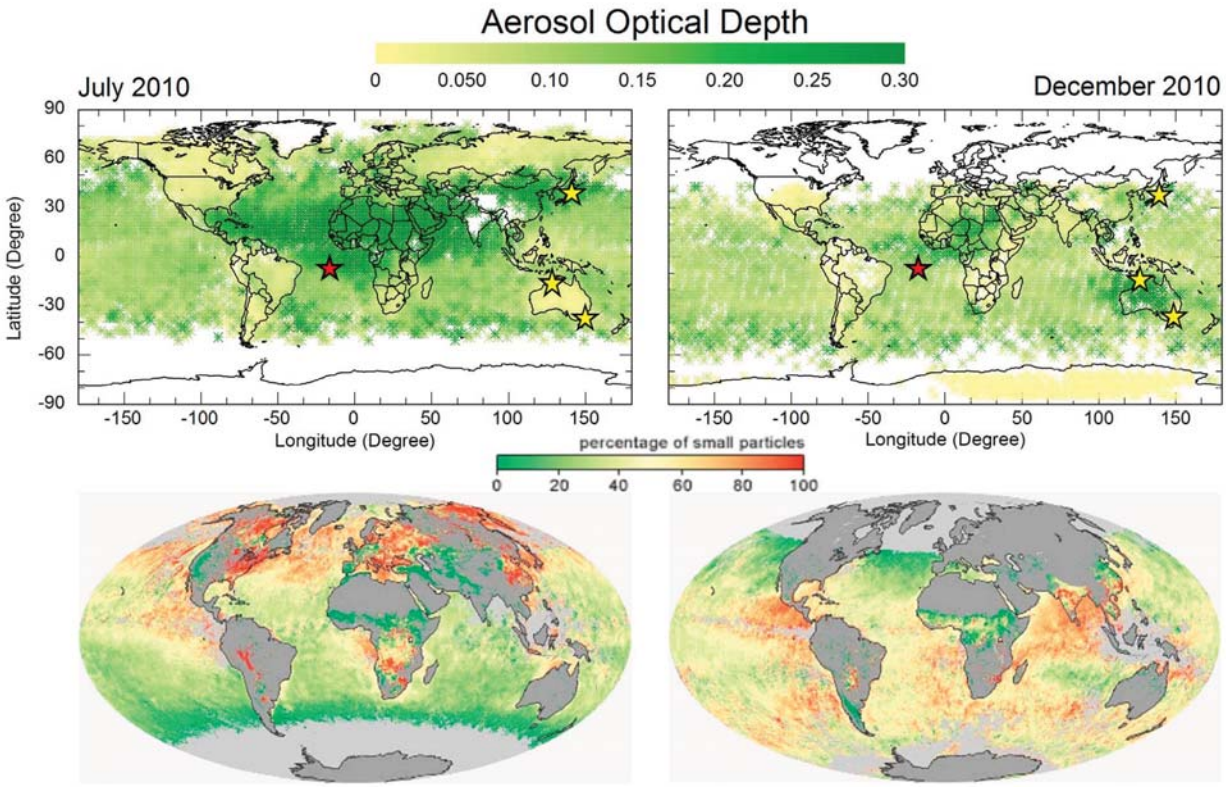


**Figure 5.** Global maps of (top) the total aerosol optical depth (AOD) from SPRINTARS and (bottom) aerosol size (in terms of the percentage of small particles) from MODIS for (left) July 2010 and (right) December 2010. The AOD data are monthly means, spatially averaged within 2.5°-latitude × 2.5°-longitude grid boxes, and values correspond to the color scales.

optical path during summer. Values of $\alpha$ are distinctly higher over Tsukuba than over Lamont, where the light path is dominantly lengthening at the seasonal maximums of the aerosol and cirrus optical depth (Figure 4, left). Although the FTS $X_{CO2}$ data at Tsukuba are rather noisy and limited to around 1 year, GOSAT PPDF-D retrievals over both Tsukuba and Lamont have similar seasonal trends and agree with the TCCON data and NIES TM results (Figure 4, top).

#### 5.1.2. Ascension Island

[49] Ascension Island is a future TCCON site [*Geibel et al.*, 2010] (ground-based FTS observations were not yet available at the time of this study). Here, we mostly demonstrate the large impact of atmospheric light scattering on GOSAT retrievals over Ascension Island when observing reflected sunlight over the ocean surface. Indeed, after the TANSO-CAI test and post-retrieval quality assessment, only 27% of GOSAT soundings were unaffected by light path modifications in the atmosphere ($\alpha$ scatter in Figure 6 (middle), section 5.2). Most GOSAT soundings over Ascension Island were related to the sun-glint observation mode. In the near-infrared region, the ocean surface is known to be dark in all directions except at the sun glint mode. For a dark surface, the detected backscattered light does not form by the photons that reach the absorbing surface; therefore, the light path tends to be shorter due to light scattering by aerosol and clouds. The sun-glint observation mode is not exempt from this rule because only a small fraction of photons reach the detector in the glint direction after being scattered by aerosol/cloud and then reflected by the surface.

[50] As a result, the effects of atmospheric light scattering shorten the path length over the ocean, and the PPDF-D retrievals underestimate $X_{CO2}$ [*Bril et al.*, 2012]. We demonstrate this in Figure 6 (top) for retrieval of the $CO_2$ amount for a set of GOSAT observations with $\alpha > 0.04$ (brown symbols). The negative bias due to shortening of the light path could be as much as $-8$ ppm.

[51] Regarding the source of the high level of atmospheric light scattering over Ascension Island, either heightened amounts of high-altitude cirrus or aerosols could shorten the light path. Figure 6 (bottom) displays seasonal variability in the aerosol optical depth calculated by SPRINTARS [*Takemura et al.*, 2000] (red histogram) and the product of the cirrus fraction by the cirrus optical depth ($\beta$) derived from the CALIOP observations [*Winker et al.*, 2007] (stars). As Figure 6 (bottom) suggests, cirrus and aerosol impacts on the optical path modifications have different seasonal variability. Whereas cirrus appears mostly between November 2009 and May 2010 (stars), which correlates seasonally with water vapor amounts (green histogram in the middle panel), the AOD has heightened values in July–August 2010 (red histogram), which is consistent with the peaks

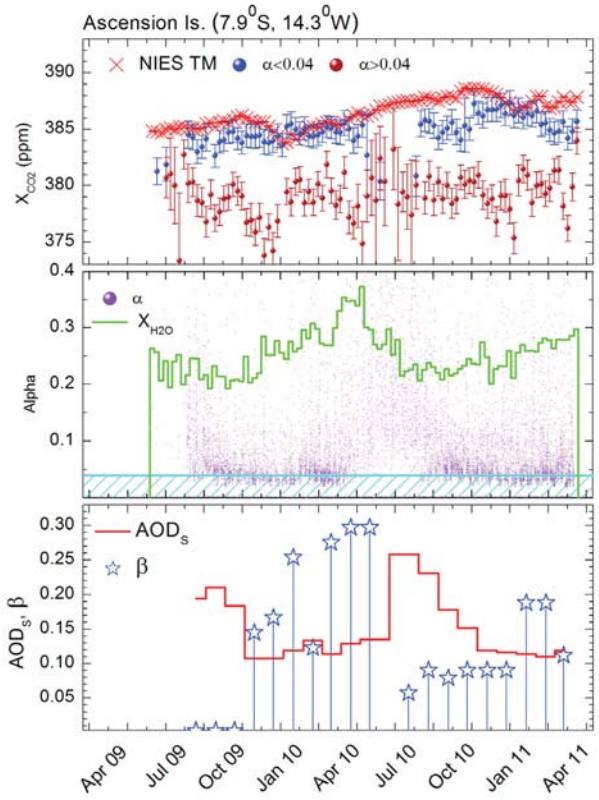


**Figure 6.** Validation of GOSAT retrievals and characteristics of atmospheric light scattering over Ascension Island (details are the same as in Figure 4). Brown symbols in the top panel display PPDF-D retrievals from GOSAT observations beyond the threshold of $\alpha > 0.04$ when shortening of the optical path leads to significant underestimation of the gas amount. For clearer display within the same axis scale, $X_{H2O}$ (mole fractions) and $\beta$ values were multiplied by factors of 50 and 10, respectively.

of $\alpha$ scatter (Figure 6, middle). Figure 5 displays global distributions of the monthly mean AOD (top) from SPRINTARS and the percentage of small particles (bottom) from the Moderate Resolution Imaging Spectroradiometer (MODIS) on NASA's Terra satellite (NASA Earth Observatory, http://earthobservatory.nasa.gov) for July 2010 (left) and December 2010 (right). The percentage of small (fine) aerosol particles was determined using the MODIS algorithm of *Remer et al.* [2005] with two aerosol modes that differ in particle size and composition (effective particle radius of 0.1 $\mu$m for fine mode and >1 $\mu$m for coarse mode). Aerosol plumes dominated by large particles can be seen over Ascension Island in July (green areas in the bottom left panel) when the AOD is significant in northern Africa and tropical regions of the Atlantic Ocean (green areas in the bottom left panel). This suggests that the light path modification over this station may largely be due to windborne mineral dust aerosols from sand storms in the Sahara and Arabian Peninsula deserts.

[52] Blue symbols in Figure 6 (top) display $X_{CO2}$ retrievals for the rest of the GOSAT soundings derived under the clearest atmospheric conditions ($\alpha < 0.04$). Although the retrievals have a small persistent negative bias of about 1–2 ppm in comparison with NIES TM, the shape of the small seasonal variations is generally in line with that of the model, at least before July 2010.

[53] When ground-based measurements at this station become available, they will be useful for testing space-based observations of greenhouse gases where light scattering by cirrus and windborne mineral dust aerosol in the sun-glint mode could significantly shorten the light path.

#### 5.1.3. Australian Stations

[54] Figure 7 displays the validation of NIES PPDF-D GOSAT data processing for two TCCON stations in Australia: Darwin (left) and Wollongong (right). As expected, the $CO_2$ retrievals show no pronounced seasonal cycle in the Southern Hemisphere, which is similar at both stations.

[55] The retrievals over the tropical Darwin station are highly contaminated by atmospheric light scattering for sun-glint observations. The summer/wet monsoonal season from December–May is very humid and dominated by marine winds [*Bouya et al.*, 2010]. The pronounced shortening of the optical path shows good correlation with the seasonal variability in water vapor column abundance (blue symbols and green histogram in Figure 7, middle left), as well as with seasonal trends in cirrus occurrence ($\beta$) and the heightened values of the AOD (stars and red histogram in Figure 7, bottom left). Most Australian deserts are located in the central and northwestern parts of the Australian continent, and winter is the dry season [*Bouya et al.*, 2010]. PPDF-D retrievals over land (black symbols in the top left panel) appear to be reasonable in comparison with ground-based FTS $X_{CO2}$ observations (green symbols in the top left panel).

[56] Similar to Tsukuba, Wollongong was one of the most difficult sites for identifying the tendency of optical path modification (Figure 7, right). The total AOD over Wollongong is lower than that over Darwin (red histograms in Figure 7, bottom). However, Wollongong is located on the outskirts of a small urban center and, as pointed out by *Wunch et al.* [2011b], the measurements at this site might be affected by local pollution. The retrieved values of the $\alpha$ and $\rho$ PPDF parameters show large variation and are frequently compatible with each other (Figure 7, middle right). The absence of a remarkable tendency in the light path modification might explain why the GOSAT data processing with simultaneous gas and aerosol/cloud retrievals over land around this site showed relatively high GOSAT $X_{CO2}$ retrieval scatter compared with other stations [*Morino et al.*, 2011; *Butz et al.*, 2011]. PPDF-D data processing over the ocean around this site showed comparatively lower scatter and bias from ground-based FTS $X_{CO2}$ (blue symbols in Figure 7, top right). Even for these observations, PPDF-based screening was found to be important, as demonstrated by the strong scatter and negative bias of $X_{CO2}$ retrieved from observations for which $\alpha > 0.04$ and thus shortening of the optical path due to aerosols or clouds over the ocean was significant (brown symbols).

### 5.2. Pairwise TCCON-GOSAT Statistical Comparison

[57] Table 1 and Figure 8 summarize the pairwise statistical comparison between GOSAT and TCCON $X_{CO2}$ data within the coincidence criterion (section 4). To statistically

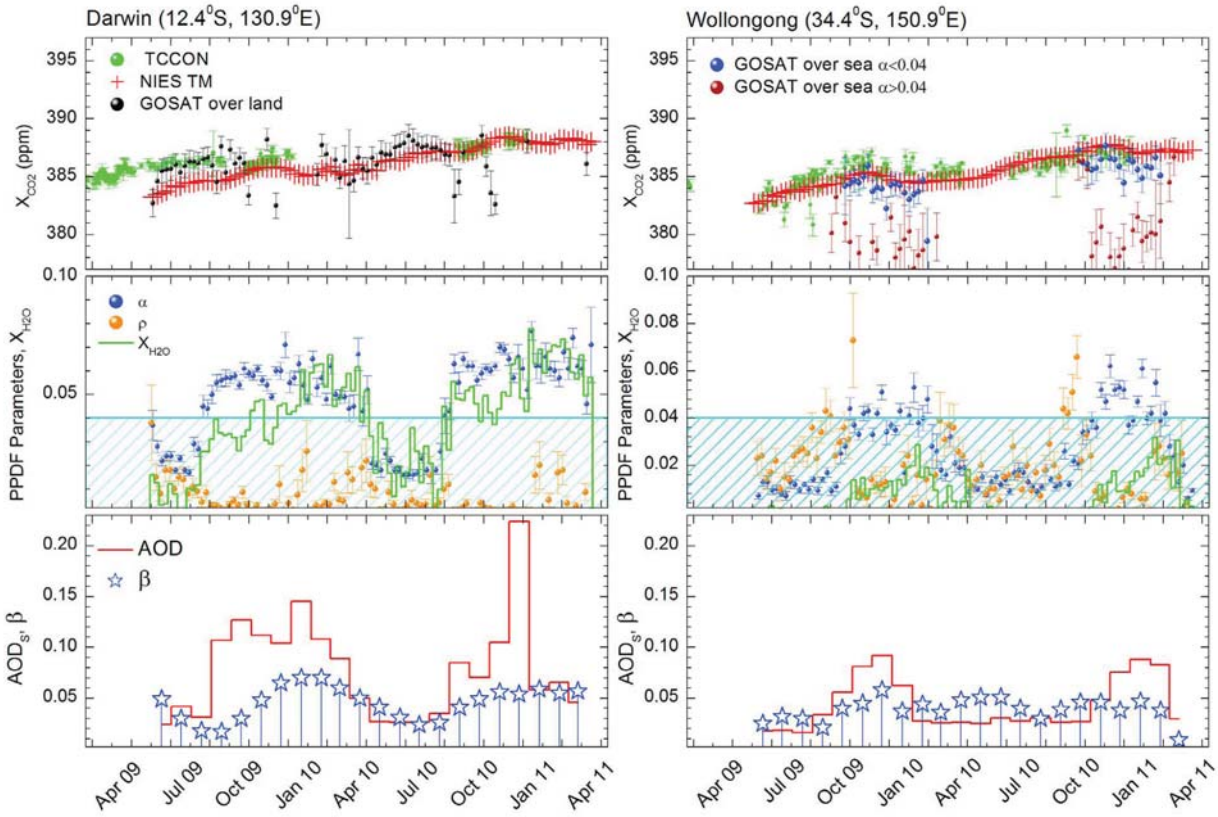


**Figure 7.** Validation of GOSAT retrievals and characteristics of atmospheric light scattering over Australian stations (left) Darwin and (right) Wollongong. Details are the same as in Figure 4. For clearer display within the same axis scale, $X_{H2O}$ (mole fractions) was multiplied by a factor of 10.

compare GOSAT ($Y_i$) and TCCON ($X_i$), mean values of $X_{CO2}$ we computed the following:

bias

$$Bias = \overline{(Y_i - X_i)}_\omega; \tag{5}$$

standard deviation

$$\sigma_{GF} = \sqrt{\left\{\overline{(Y_i - X_i - Bias)^2}\right\}_\omega}; \tag{6}$$

Pearson's correlation coefficient

$$r = \frac{\left\{\overline{(X_i - \bar{X}_\omega)(Y_i - \bar{Y}_\omega)}\right\}_\omega}{\sqrt{\left\{\overline{(X_i - \bar{X}_\omega)^2}\right\}_\omega \left\{\overline{(Y_i - \bar{Y}_\omega)^2}\right\}_\omega}}; \tag{7}$$

coefficient of determination (goodness of fit)

$$R^2 = 1 - \frac{\left\{\overline{(Y_i - y_i)^2}\right\}_\omega}{\left\{\overline{(Y_i - \bar{Y}_\omega)^2}\right\}_\omega}; \tag{8}$$

where $y_i$ denotes the least squares-adjusted points (expectation values of $Y_i$) in the best linear fit between the GOSAT and TCCON $X_{CO2}$ mean values according to *York et al.* [2004]. This technique effectively accounts for uncertainties in both the $Y_i$ and $X_i$ data sets when they vary from point to point. The mean values $\bar{Z}_\omega = (\sum_i \omega_i)^{-1} \sum_i \omega_i z_i$ in equations (5)–(8) are weighted as

$$\omega_i = \frac{\omega_i^F \cdot \omega_i^G}{\omega_i^F + a^2 \omega_i^G}, \tag{9}$$

through standard deviations $\sigma_i^G$ and $\sigma_i^F$ ($\omega = \frac{1}{\sigma^2}$) of uncorrelated GOSAT ($Y_i$) and TCCON ($X_i$) mean values. In equation (9) $a$ is the regression slope, which is known to be an important measure when characterizing the bias correction. The slope values and their errors ($1\sigma$) are listed in Table 1. For each TCCON station, we also tabulated the following:

[58] $N_S$ – the total number of GOSAT single scans available after the quality assessment (section 2.2), application of $X_{CO2}$ selection criterion (section 4), and PPDF screening (section 2.2);

[59] $R_{\%}$ – remaining percentage of GOSAT single scans after PPDF-based screening;

[60] $N_C$ – the total number of GOSAT single scans coincident with TCCON measurements, after quality assessment and application of $X_{CO2}$ selection criterion; and

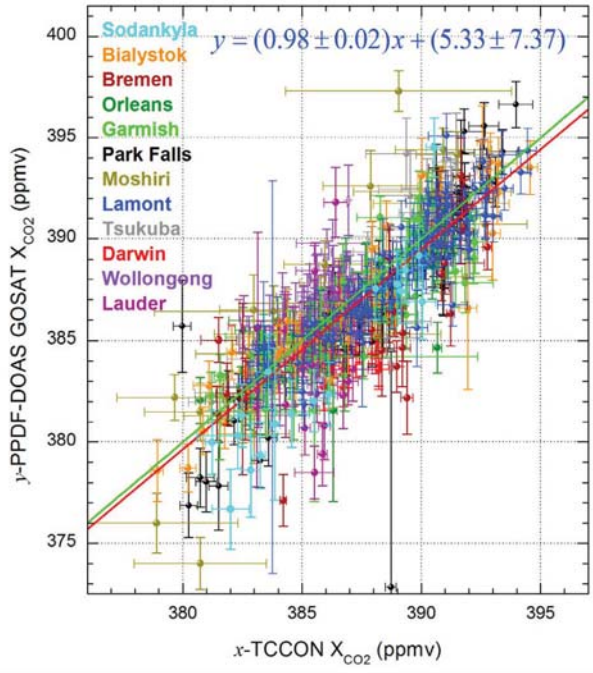


**Figure 8.** Correlation diagram between GOSAT and ground-based FTS measurements of $X_{CO2}$. The GOSAT data were selected within 15°-latitude × 45°-longitude grid boxes centered over each FTS station. The analyzed ground-based FTS data were mean values measured within 1 h of the GOSAT overpass time, and both GOSAT and TCCON data were averaged weekly. Red lines correspond to the best fit for all sites (with the fitting equation given in the inset) and the green line representing one-to-one correspondence. The number of available GOSAT soundings and characteristics of statistical relationships between ground-based FTS and GOSAT $X_{CO2}$ for each TCCON station are listed in Table 1.

[61] $N_a$ – the number of coincident GOSAT and TCCON mean values of $X_{CO2}$.

[62] Statistical characteristics are listed in Table 1 for each TCCON site, as well as summarized separately for stations in the Northern and Southern hemispheres. The last row in Table 1 represents the data for all TCCON sites. Slope $a$, correlation coefficients (7), and coefficients of determination (8) are not summarized in Table 1 for three operational stations in the Southern Hemisphere (blank cells) due to the low variability in $X_{CO2}$, but both GOSAT and TCCON data for these sites were included when estimating these quantities for all operational sites (last row in Table 1). Incorporation of data from the Southern Hemisphere into the total data set had little impact on the slope of the linear regression, but noticeably degraded the correlation coefficients and standard deviations between GOSAT and TCCON observations. The best values of the slope were for Lamont and Bialystok (1.01); ∼0.1 deviation of the slope from unity were found for the Bremen and Garmisch sites. We believe that the relatively high deviation of the slope from unity ($|a| > 1$) for Sodankyla, Moshiri, and Tsukuba was due to insufficient numbers (<300) of coincident GOSAT and TCCON observations for proper statistical analysis; this could also explain the largest bias in $X_{CO2}$ over Moshiri site and the lowest correlation coefficient over Bremen site. The close correlation of GOSAT observations with TCCON measurements over Tsukuba and Moshiri is not representative and mostly attributable to the large uncertainties in $X_{CO2}$ at these TCCON stations (green bars in Figure 4 for the Tsukuba site).

[63] The clearest atmosphere within the available set of GOSAT $N_S$ observations was over Lamont ($R_{\%}$ = 76%) and Sodankyla ($R_{\%}$ = 77%; Table 1). Note again that this assessment concerns only PPDF-based screening ($\alpha$, $\rho < 0.04$) of the initial GOSAT soundings that were filtered by the CAI prescreening test (section 2.1) and passed the GOSAT data and retrieval quality assessment (section 2.2). The smallest number of remaining scans with negligible light path modification was detected in the Southern Hemisphere stations over Ascension Island ($R_{\%}$ = 27%) and Lauder ($R_{\%}$ = 30%). We discussed possible reasons for the high level of atmospheric light scattering over Ascension Island in section 5.1.2. As noted by *Liley and Forgan* [2009], the aerosol optical depth data obtained continuously over Lauder since 1999 are among the lowest observed worldwide. The SPRINTARS model also showed fairly low values of AOD during the 22 months of GOSAT observations considered in this study. We have no explanation for the large light path modifications around this station, except for the presence of elevated subvisible cirrus. The maximal value of $\beta$ = 0.055 (the product of the cirrus fraction by cirrus optical depth from CALIOP observations) was detected in November–December 2009 and is noticeably larger than that over Ascension Island ($\beta$ = 0.017 in the same period). This example shows that the total aerosol optical depth is not always a sufficiently representative quantity to characterize the possible impact of atmospheric light scattering when retrieving gas amounts from space [*Oshchepkov et al.*, 2011].

[64] For the coincident measurements over all stations, GOSAT and TCCON data of $CO_2$ column abundance showed a correlation coefficient of 0.85, standard deviation of 1.80 ppm, and a sub-ppm negative bias of −0.43 ppm. For the Northern Hemisphere sites, where pronounced seasonal trends provide larger variability in $X_{CO2}$, these statistical characteristics were 0.90, 1.65 ppm, and −0.47 ppm, respectively (Table 1).

### 5.3. Global Distribution of $CO_2$

[65] Figure 9 displays a comparison between the global distributions of $CO_2$ monthly mean column abundance calculated with NIES TM (right panels) and those retrieved from GOSAT data processing (left panels represent the retrievals as deviation from the modeled values). The modeled data shown in Figure 9 were generated only for the locations of those GOSAT soundings that passed through the CAI prescreening test (section 2.1) and also passed the GOSAT data and retrieval quality assessment (section 2.2). This results in some gaps in the NIES $X_{CO2}$ monthly averages. To produce these maps, we did not apply weighted interpolation, such as by the kriging technique; we simply calculated the spatial average of $X_{CO2}$ values within 2.5°-latitude × 2.5°-longitude grid boxes and excluded cases in

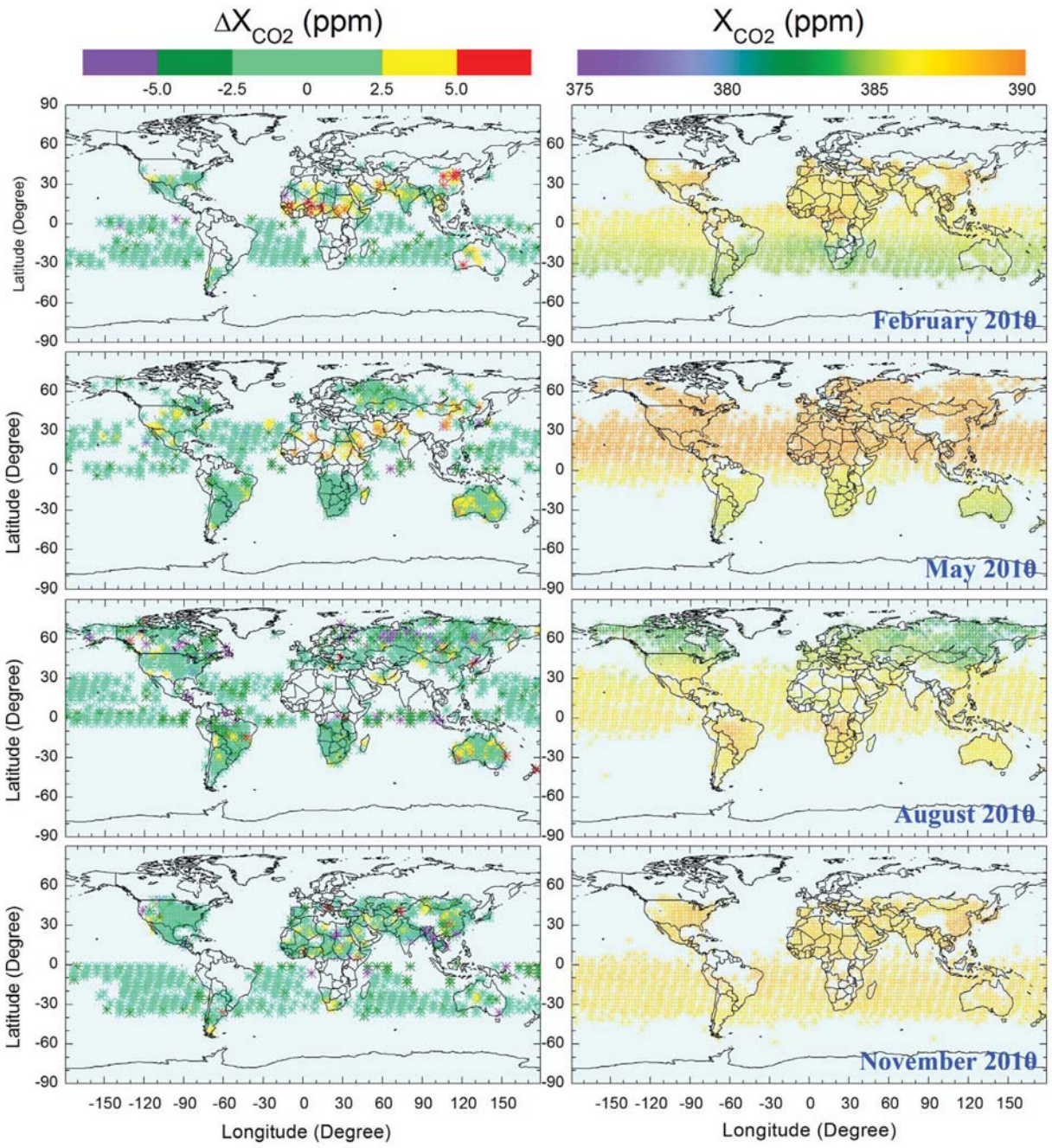


**Figure 9.** Global maps of the monthly mean $X_{CO2}$ (values (ppm) correspond to the color scales) (left) from NIES TM and (right) from GOSAT data processing in terms of deviation $\Delta X_{CO2} = X_{CO2}^{GOSAT} - X_{CO2}^{Model}$ from (top to bottom) February–November 2010. The data are averaged over 2.5°-latitude × 2.5°-longitude grid boxes.

which only one scan fell into the grid box as unrepresentative data.

[66] The period covers 10 months of GOSAT observations in 2010 (every 3 months from February–November 2010). These months were selected because they reflect significant temporal and spatial $X_{CO2}$ variability. In particular, the $X_{CO2}$ latitudinal gradient changes sign between February and August; the highest amount of $CO_2$ in the Northern Hemisphere is in May; and a comparatively homogeneous global distribution of $CO_2$ can be observed in November, with considerable enhancement of $CO_2$ amount in the eastern parts of the USA and China (Figure 9).

[67] The global distribution of retrieved $X_{CO2}$ reasonably reproduces the column abundance derived from NIES TM (Figure 9, right). The displayed deviations $\Delta X_{CO2} = X_{CO2}^{GOSAT} - X_{CO2}^{Model}$ between retrieved $X_{CO2}^{GOSAT}$ and modeled

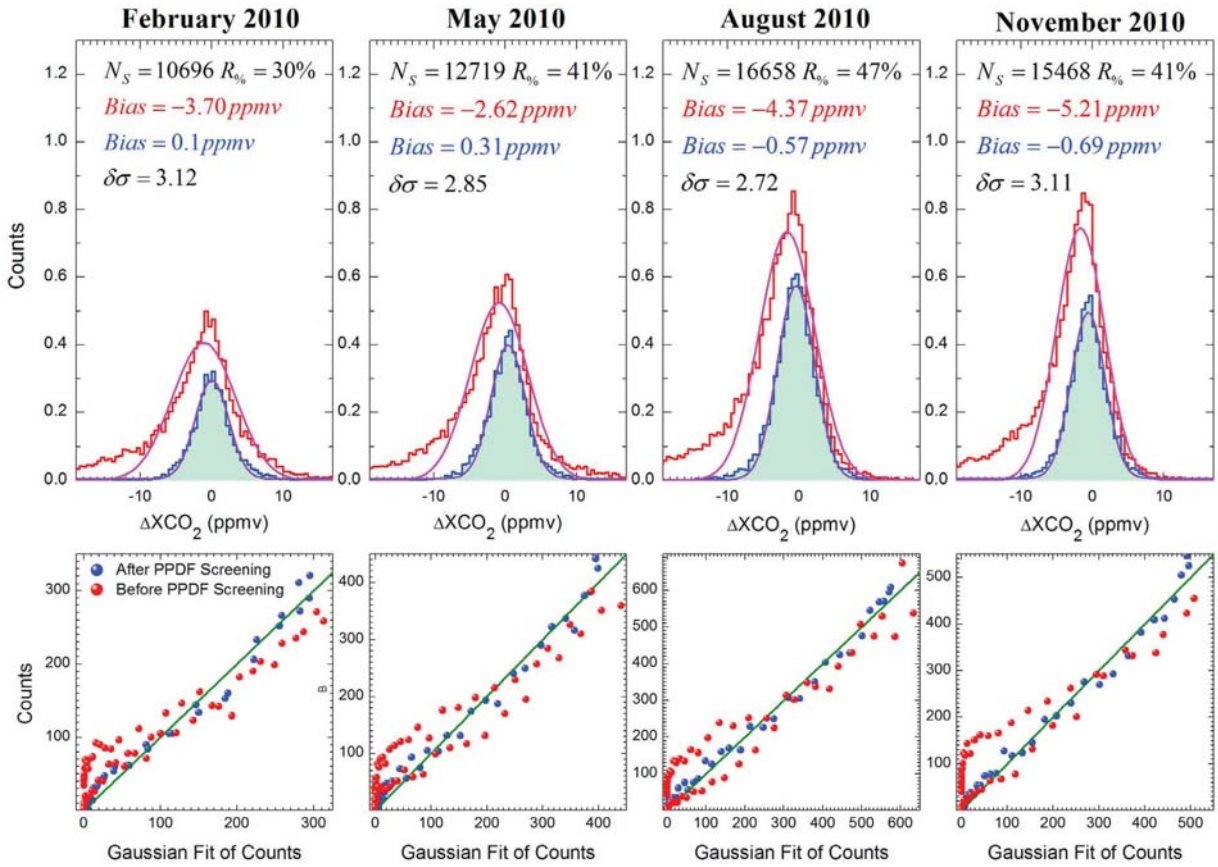


**Figure 10.** Statistical distributions of GOSAT single soundings by deviation between retrieved and modeled $CO_2$ column abundance. Each panel corresponds to global data obtained within 1 month. (top) Distribution of GOSAT counts (multiplied by a factor of 0.001) by $\Delta X_{CO2}$ before (red) and after (blue) PPDF-based screening. Histograms represent original data and lines correspond to the best fit by Gaussian distributions. (bottom) Correlation diagrams between original counts and those derived from Gaussian fitting at intervals of 0.5 ppm. Distance of points from the green line (one-to-one correspondence line) reflects the quality of the fitting.

$X_{CO2}^{Model}$ values are mostly within 2.5 ppm (±0.5%), according to the color scale (light green). We display the modeled data for the GOSAT soundings that satisfied the instrumental and retrieval quality assessment (section 2.2). The retrievals were additionally filtered by PPDF-based screening. The results of screening can be seen by comparing the spatial covering of $X_{CO2}$ in Figure 9 (left and right); most of the spatial gaps that result from excluding observations were over northern Africa and tropical ocean regions, as seen in the left panel, suggesting that light path modification due to atmospheric light scattering was large for these observations.

[68] Figure 10 shows statistics of monthly global GOSAT single soundings distributed by the deviation $\Delta X_{CO2}$ (blue histograms). Blue lines correspond to the best fit of the original data to Gaussian distribution $\mathcal{N}(\Delta X_{CO2};\ \mu,\ \sigma^2)$ with zero vertical offset [ $\lim_{(\Delta X_{CO2}-\mu)\to\infty}(\mathcal{N}) \to 0$]. For comparison, we also plot the same type of distributions for GOSAT soundings that were not filtered by PPDF-based screening (red histograms and lines). Whereas the fit of filtered data is rather good, the distributions of GOSAT observations contaminated by light path modification tend to be asymmetrical, with remarkable enhancement of the counts at negative values of $\Delta X_{CO2}$. Correlation diagrams between the original counts and the Gaussian fit at intervals of 0.5 ppm shown in Figure 10 (bottom) illustrate the quality of the fits: deviation of blue points from the green line of one-to-one correspondence is much lower than that of red points. The asymmetrical shape of GOSAT counts before PPDF-based screening (red lines in Figure 10) is evidently due to atmospheric light scattering over the dark surface (mostly over the ocean) that leads to shortening of the optical path and, hence, to underestimation of the gas amount ($\Delta X_{CO2} < 0$). The negative bias between retrieved and modeled $X_{CO2}$ could reach up to −5 ppm, whereas the deviation for post-screening data is <1 ppm ("*Bias*" in insets of Figure 10). The insets in Figure 10 also show the decrease, $\delta\sigma$, in the standard deviation $\sigma$ (equation (6)) due to PPDF-based screening, $\delta\sigma = \sigma_b/\sigma_a$, where subscripts $b$ and $a$ denote "before" and "after" the screening, respectively. On average, the standard deviation reduces to about 30%.

[69] These results suggest that PPDF-based screening is an efficient way to significantly reduce biases and standard deviations in retrieving $CO_2$ column abundance on a global scale. After this screening, the remaining scatter would be due to the combination of a large number of random variables (blue histograms obey Gaussian distributions in Figure 10). Spatial averaging of the retrievals, such as those presented in Figure 9, provides sub-ppm monthly mean global bias when compared with NIES TM.

## 6. Summary and Concluding Remarks

[70] GOSAT TANSO-FTS SWIR spectra were processed with a PPDF-based method of $X_{CO2}$ and optical path retrievals during 22 months from June 2009. As part of this GOSAT validation study, we compared the retrieved $CO_2$ column abundance seasonally against reference $X_{CO2}$ data derived from TCCON ground-based FTS measurements and globally against $X_{CO2}$ from an atmospheric tracer transport model simulations. We also analyzed seasonal variability in the effects of atmospheric light scattering over each TCCON station through retrievals of the optical path modifications.

[71] For representative statistical comparison between TCCON and GOSAT observations, we collected weekly mean GOSAT data within 15°- latitude × 45°-longitude grid boxes centered over each TCCON station. To constrain the natural variability in $CO_2$ within each pixel, we excluded observations for which the NIES TM showed >1 ppm difference in $CO_2$ column abundance from that of the TCCON site. For temporal correspondence, the ground-based TCCON measurements were limited to within 1 h of the GOSAT overpass time for each station. This provided a large sample of GOSAT observations that were over both land and ocean.

[72] An effect of optical path lengthening was found over most Northern Hemisphere stations, essentially from June–September each year. On the other hand, an effect of optical path shortening was found for sun-glint observations over ocean in tropical regions. The detected effects in light path modification were physically interpreted and supported by the seasonal trends of the aerosol optical depth derived from an offline three-dimensional aerosol transport model (SPRINTARS), as well as by the time series of cirrus optical depth (weighted by the cirrus fraction) derived from space-based lidar measurements by the CALIOP instrument onboard CALIPSO. Removal of these observations from the GOSAT data set led to acceptable agreement in the seasonal variability of $CO_2$ retrievals with TCCON measurements over most stations.

[73] As noted in section 4, we conducted L1B data processing on GOSAT soundings that had already been filtered by the TANSO-CAI prescreening test. Within this data set, the smallest light path modifications were detected over the Lamont ($R_{\%}$ = 76%) and Sodankyla ($R_{\%}$ = 77%) stations and the largest modifications were found in Southern Hemisphere sites over Ascension Island ($R_{\%}$ = 27%) and Lauder ($R_{\%}$ = 30%).

[74] Statistical pairwise comparison between GOSAT and TCCON coincident measurements of $CO_2$ column abundance showed a slope of 0.98 for the slope-intercept form of the linear regression, a correlation coefficient of 0.85, a coefficient of determination of 0.78, a standard deviation of 1.80 ppm, and a sub-ppm negative bias of 0.43 ppm over all 12 TCCON sites. For the nine stations in the Northern Hemisphere where seasonal and regional variability in $CO_2$ amount were more pronounced, most of the abovementioned statistical characteristics were improved.

[75] This study demonstrates that PPDF-based screening is an efficient way to significantly reduce the bias and standard deviation in retrieving $CO_2$ column abundance on a global scale. In particular, global distributions of the monthly mean retrieved $CO_2$ column abundance with a spatial resolution of 2.5°-latitude × 2.5°-longitude grid boxes generally agreed well with the distributions predicted by the atmospheric tracer transport model.

[76] As noted in section 2.2, this paper deals with PPDF retrieval in the oxygen A-band (0.76 $\mu$m) only as a prescreening step to remove GOSAT soundings that are highly contaminated by light path modification. Then, the remaining GOSAT soundings are processed to retrieve $CO_2$ amounts in gas bands 2 (1.61 $\mu$m) and 3 (2.0 $\mu$m) using the simplified equation (2) for the effective transmittance with zero PPDF parameters. This method is mainly used because of the significant difference in PPDFs between the GOSAT bands due to the spectral variability in aerosol and cloud optical characteristics as well as ground-surface albedo. Simultaneous retrieval of PPDF parameters and gas amount using all available GOSAT SWIR bands is currently underway in the NIES GOSAT project.

[77] The temporal and spatial variability in optical path modification reported in this study would be valuable for testing any other retrieval algorithm that aims to simultaneously retrieve gas amounts and aerosol or cloud optical characteristics. In particular, the statistical distribution of GOSAT single scans available after data processing by light path modifications could aid in testing the quality of retrievals when the simultaneous retrieval of aerosol and cloud characteristics is essential. We address this important issue in the next part of our companion paper which also includes algorithms intercomparison.

[78] **Acknowledgments.** GOSAT is a joint effort of the Japan Aerospace Exploration Agency (JAXA), the National Institute for Environmental Studies (NIES), and the Ministry of the Environment (MOE), Japan. U.S. funding for TCCON is provided by NASA's Terrestrial Ecology Program (grant NNX11AG01G), the Orbiting Carbon Observatory Program, the Atmospheric $CO_2$ Observations from Space (ACOS) Program, and the Department of Energy/Atmospheric Radiation Measurement (DOE/ARM) Program. The Darwin TCCON site was built at Caltech with funding from the OCO project, and is operated by the University of Wollongong, with travel funds for maintenance and equipment costs funded by the OCO-2 project. We acknowledge funding to support Darwin and Wollongong from the Australian Research Council, projects LE0668470, DP0879468, DP110103118 and LP0562346. Lauder TCCON measurements are funded by New Zealand Foundation of Research Science and Technology contracts C01X0204 and CO1X0406. We acknowledge financial support of the Białystok and Orléans TCCON sites from the Senate of Bremen and EU projects IMECC, GEOMON and InGOS as well as maintenance and logistical work provided by AeroMeteo Service (Białystok) and the RAMCES team at LSCE (Gif-sur-Yvette, France) and additional operational funding from the NIES GOSAT project. The Garmisch TCCON team acknowledges funding by the EC-INGOS project. We acknowledge the CALIOP mission for obtaining the cloud data. The JRA-25/JCDAS data sets used for atmospheric transport modeling were provided by the cooperative, long-term reanalysis project by the Japan Meteorological Agency (JMA) and Central Research

Institute of Electric Power Industry (CRIEPI). The authors thank Yasuhiro Sasano, Director of the Center for Global Environmental Research at the NIES, the members of the NIES GOSAT and NASA ACOS projects, and three anonymous reviewers for their helpful comments.

## References


Aben, I., O. Hasekamp, and W. Hartmann (2007), Uncertainties in the space-based measurements of $CO_2$ columns due to scattering in the Earth's atmosphere, *J. Quant. Spectrosc. Radiat. Transfer*, *104*, 450–459, doi:10.1016/j.jqsrt.2006.09.013.

Belikov, D., et al. (2011), Mass-conserving tracer transport modeling on a reduced latitude-longitude grid with NIES-TM, *Geosci. Model Dev.*, *4*, 207–222, doi:10.5194/gmd-4-207-2011.

Belikov, D., et al. (2012), Simulations of column-average $CO_2$ and $CH_4$ using the NIES TM with a hybrid sigma-isentropic ($\sigma$-$\theta$) vertical coordinate, *Atmos. Chem. Phys. Discuss.*, *12*, 8053–8106, doi:10.5194/acpd-12-8053-2012.

Bennartz, R., and R. Preusker (2006), Representation of the photon path-length distribution in a cloudy atmosphere using finite elements, *J. Quant. Spectrosc. Radiat. Transfer*, *98*, 202–219, doi:10.1016/j.jqsrt.2005.05.085.

Boden, T. A., G. Marland, and R. J. Andres (2009), *Global, Regional, and National Fossil Fuel $CO_2$ Emissions*, Carbon Dioxide Inf. Anal. Center, Oak Ridge Natl. Lab., U.S. Dep. of Energy, Oak Ridge, Tenn.

Bösch, H., et al. (2006), Space-based near-infrared $CO_2$ measurements: Testing the Orbiting Carbon Observatory retrieval algorithm and validation concept using SCIAMACHY observations over Park Falls, Wisconsin, *J. Geophys. Res.*, *111*, D23302, doi:10.1029/2006JD007080.

Bouya, Z., G. P. Box, and M. A. Box (2010), Seasonal variability of aerosol optical properties in Darwin, Australia, *J. Atmos. Sol. Terr. Phys.*, *72*, 726–739, doi:10.1016/j.jastp.2010.03.015.

Bril, A., S. Oshchepkov, T. Yokota, and G. Inoue (2007), Parameterization of aerosol and cirrus cloud effects on reflected sunlight spectra measured from space: Application of the equivalence theorem, *Appl. Opt.*, *46*, 2460–2470, doi:10.1364/AO.46.002460.

Bril, A., S. Oshchepkov, and T. Yokota (2012), Application of a probability density function-based atmospheric light-scattering correction to carbon dioxide retrievals from GOSAT over-sea observations, *Remote Sens. Environ.*, *117*, 301–306, doi:10.1016/j.rse.2011.10.005.

Buchwitz, M., V. Rozanov, and J. P. Burrows (2000), A near-infrared optimized DOAS method for the fast global retrieval of atmospheric $CH_4$, CO, $CO_2$, $H_2O$, and $N_2O$ total column amounts from SCIAMACHY Envisat-1 nadir radiances, *J. Geophys. Res.*, *105*, 15,231–15,245, doi:10.1029/2000JD900191.

Butz, A., O. P. Hasekamp, C. Frankenberg, and I. Aben (2009), Retrievals of atmospheric $CO_2$ from simulated space-borne measurements of backscatter near-infrared sunlight: Accounting for aerosol effects, *Appl. Opt.*, *48*, 3322–3336, doi:10.1364/AO.48.003322.

Butz, A., et al. (2011), Toward accurate $CO_2$ and $CH_4$ observations from GOSAT, *Geophys. Res. Lett.*, *38*, L14812, doi:10.1029/2011GL047888.

Chevallier, F., F.-M. Br'eon, and P. J. Rayner (2007), Contribution of the Orbiting Carbon Observatory to the estimation of $CO_2$ sources and sinks: Theoretical study in a variational data assimilation framework, *J. Geophys. Res.*, *112*, D09307, doi:10.1029/2006JD007375.

Chevallier, F., S. Maksyutov, P. Bousquet, F.-M. Bréon, R. Saito, Y. Yoshida, and T. Yokota (2009), On the accuracy of the $CO_2$ surface fluxes to be estimated from the GOSAT observations, *Geophys. Res. Lett.*, *36*, L19807, doi:10.1029/2009GL040108.

Connor, B. J., H. Boesch, G. Toon, B. Sen, C. Miller, and D. Crisp (2008), Orbiting Carbon Observatory: Inverse method and prospective error analysis, *J. Geophys. Res.*, *113*, D05305, doi:10.1029/2006JD008336.

Deutscher, N. M., et al. (2010), Total column $CO_2$ measurements at Darwin, Australia—Site description and calibration against in situ aircraft profiles, *Atmos. Meas. Tech.*, *3*(4), 947–958, doi:10.5194/amt-3-947-2010.

Dufour, E., and F.-M. Bréon (2003), Spaceborne estimate of atmospheric $CO_2$ column by use of the differential absorption method: Error analysis, *Appl. Opt.*, *42*, 3595–3609, doi:10.1364/AO.42.003595.

Frankenberg, C., U. Platt, and T. Wagner (2005), Iterative maximum a posteriori (IMAP)-DOAS for retrieval of strongly absorbing trace gases: Model studies for $CH_4$ and $CO_2$ retrieval from near infrared spectra of SCIAMACHY onboard ENVISAT, *Atmos. Chem. Phys.*, *5*, 9–22, doi:10.5194/acp-5-9-2005.

Geibel, M. C., C. Gerbig, and D. G. Feist (2010), A new fully automated FTIR system for total column measurements of greenhouse gases, *Atmos. Meas. Tech.*, *3*, 1363–1375.

GLOBALVIEW-$CO_2$ (2010), Cooperative Atmospheric Data Integration Project—Carbon Dioxide [CD-ROM], NOAA Earth Syst. Res. Lab., Boulder, Colo. [Available at ftp.cmdl.noaa.gov, path: Ccg/co2/GLOBALVIEW.]

Gurney, K. R., et al. (2004), Transcom 3 inversion intercomparison: Model mean results for the estimation of seasonal carbon sources and sinks, *Global Biogeochem. Cycles*, *18*, GB1010, doi:10.1029/2003GB002111.

Hamazaki, T., Y. Kaneko, A. Kuze, and K. Kondo (2005), Fourier transform spectrometer for greenhouse gases observing satellite (GOSAT), *Proc. SPIE*, *5659*, 73, doi:10.1117/12.581198.

Intergovernmental Panel on Climate Change (2007), *Climate Change 2007: The Physical Science Basis: Contribution of Working Group I to the Fourth Assessment Report of the Intergovernmental Panel on Climate Change*, edited by S. Solomon et al., Cambridge Univ. Press, Cambridge, U. K.

Ishida, H., and T. Y. Nakajima (2009), Development of an unbiased cloud detection algorithm for a spaceborne multispectral imager, *J. Geophys. Res.*, *114*, D07206, doi:10.1029/2008JD010710.

Kadygrov, N., S. Maksyutov, N. Eguchi, T. Aoki, T. Nakazawa, T. Yokota, and G. Inoue (2009), Role of simulated GOSAT total column $CO_2$ observations in surface $CO_2$ flux uncertainty reduction, *J. Geophys. Res.*, *114*, D21208, doi:10.1029/2008JD011597.

Keppel-Aleks, G., P. O. Wennberg, and T. Schneider (2011), Sources of variations in total column carbon dioxide, *Atmos. Chem. Phys.*, *11*, 3581–3593, doi:10.5194/acp-11-3581-2011.

Kuze, A., H. Suto, M. Nakajima, and T. Hamazaki (2009), Thermal and near infrared sensor for carbon observation Fourier-transform spectrometer on the Greenhouse Gases Observing Satellite for greenhouse gases monitoring, *Appl. Opt.*, *48*, 6716–6733, doi:10.1364/AO.48.006716.

Liley, J. B., and B. W. Forgan (2009), Aerosol optical depth over Lauder, New Zealand, *Geophys. Res. Lett.*, *36*, L07811, doi:10.1029/2008GL037141

Maksyutov, S., et al. (2008), NIES/FRCGC global atmospheric tracer transport model: Description, validation, and surface sources and sinks inversion, *J. Earth Simulator*, *9*, 3–18.

Mao, J., and S. R. Kawa (2004), Sensitivity studies for space-based measurement of atmospheric total column carbon dioxide by reflected sunlight, *Appl. Opt.*, *43*, 914–927, doi:10.1364/AO.43.000914.

Messerschmidt, J., et al. (2010), Side by side measurements of $CO_2$ by ground-based Fourier transform spectrometry (FTS), *Tellus, Ser. B*, *62*, 749–758, doi:10.1111/j.1600-0889.2010.00491.x.

Miyazaki, K., P. K. Patra, M. Takigawa, T. Iwasaki, and T. Nakazawa (2008), Global-scale transport of carbon dioxide in the troposphere, *J. Geophys. Res.*, *113*, D15301, doi:10.1029/2007JD009557.

Morino, I., et al. (2011), Preliminary validation of column-averaged volume mixing ratios of carbon dioxide and methane retrieved from GOSAT short-wavelength infrared spectra, *Atmos. Meas. Tech.*, *4*, 1061–1076, doi:10.5194/amt-4-1061-2011.

Nakajima, T., et al. (2008), A study of aerosol and cloud information retrievals from CAI imager on board GOSAT satellite [in Japanese with English abstract and figure captions], *J. Remote Sens. Soc. Jpn.*, *28*, 178–189.

Niwa, Y., et al. (2011), Three-dimensional variations of atmospheric $CO_2$: Aircraft measurements and multi-transport model simulations, *Atmos. Chem. Phys.*, *11*, 13,359–13,375, doi:10.5194/acp-11-13359-2011.

O'Brien, D. M., and P. J. Rayner (2002), Global observations of the carbon budget: 2. $CO_2$ column from differential absorption of reflected sunlight in the 1.61 $\mu$m band of $CO_2$, *J. Geophys. Res.*, *107*(D18), 4354, doi:10.1029/2001JD000617.

O'Dell, C. W., et al. (2012), The ACOS $CO_2$ retrieval algorithm—Part 1: Description and validation against synthetic observations, *Atmos. Meas. Tech.*, *5*, 99–121, doi:10.5194/amt-5-99-2012.

Olivier, J. G. J., and J. J. M. Berdowski (2001), *Global Emissions Sources and Sinks*, A. A. Balkema, Lisse, Netherlands.

Onogi, K., et al. (2007), The JRA-25 reanalysis, *J. Meteorol. Soc. Jpn.*, *85* (3), 369–432, doi:10.2151/jmsj.85.369.

Oshchepkov, S., A. Bril, and T. Yokota (2008), PPDF-based method to account for atmospheric light scattering in observations of carbon dioxide from space, *J. Geophys. Res.*, *113*, D23210, doi:10.1029/2008JD010061.

Oshchepkov, S., A. Bril, and T. Yokota (2009), An improved photon path length probability density function-based radiative transfer model for space-based observation of greenhouse gases, *J. Geophys. Res.*, *114*, D19207, doi:10.1029/2009JD012116.

Oshchepkov, S., A. Bril, S. Maksyutov, and T. Yokota (2011), Detection of optical path in spectroscopic space-based observations of greenhouse gases: Application to GOSAT data processing, *J. Geophys. Res.*, *116*, D14304, doi:10.1029/2010JD015352.

Patra, P. K., et al. (2011), TransCom model simulations of $CH_4$ and related species: Linking transport, surface flux and chemical loss with $CH_4$ variability in the troposphere and lower stratosphere, *Atmos. Chem. Phys. Discuss.*, *11*, 18,767–18,821, doi:10.5194/acpd-11-18767-2011.

Rayner, P. J., and D. M. O'Brien (2001), The utility of remotely sensed $CO_2$ concentration data in surface source inversions, *Geophys. Res. Lett.*, *28*, 175–178, doi:10.1029/2000GL011912.

Remer, L. A., et al. (2005), The MODIS aerosol algorithm, products, and validation, *J. Atmos. Sci.*, *62*(4), 947–973, doi:10.1175/JAS3385.1.

Reuter, M., M. Buchwitz, O. Schneising, J. Heymann, H. Bovensmann, and J. P. Burrows (2010), A method for improved SCIAMACHY $CO_2$ retrieval in the presence of optically thin clouds, *Atmos. Meas. Tech.*, *3*, 209–232, doi:10.5194/amt-3-209-2010.

Rodgers, C. D. (2000), *Inverse Methods for Atmospheric Sounding: Theory and Practice*, World Sci, Singapore, doi:10.1142/9789812813718.

Shimizu, A., N. Sugimoto, I. Matsui, K. Arao, I. Uno, T. Murayama, N. Kagawa, K. Aoki, A. Uchiyama, and A. Yamazaki (2004), Continuous observations of Asian dust and other aerosols by polarization lidars in China and Japan during ACE-Asia, *J. Geophys. Res.*, *109*, D19S17, doi:10.1029/2002JD003253.

Takemura, T., H. Okamoto, Y. Maruyama, A. Numaguti, A. Higurashi, and T. Nakajima (2000), Global three-dimensional simulation of aerosol optical thickness distribution of various origins, *J. Geophys. Res.*, *105*, 17,853–17,873, doi:10.1029/2000JD900265.

Tiedtke, M. (1989), A comprehensive mass flux scheme for cumulus parameterization in large scale models, *Mon. Weather Rev.*, *117*, 1779–1800, doi:10.1175/1520-0493(1989)117<1779:ACMFSF>2.0.CO;2.

Toon, G. C. (1992), Composition measurements of the 1989 Arctic winter stratosphere by airborne infrared solar absorption spectroscopy, *J. Geophys. Res.*, *97*, 7939–7961, doi:10.1029/91JD03114.

Watanabe, H., A. Yuki, K. Hayashi, F. Kawazoe, N. Kikuchi, F. Takahashi, T. Matsunaga, and T. Yokota (2010), GOSAT higher level product status 1.5 year after the launch, *Proc. SPIE*, *7826*, 782606, doi:10.1117/12.865577.

Winker, D. M., W. H. Hunt, and M. J. McGill (2007), Initial performance assessment of CALIOP, *Geophys. Res. Lett.*, *34*, L19803, doi:10.1029/2007GL030135.

World Data Centre for Greenhouse Gases (2011), WMO Global Watch World Data Centre for Greenhouse Gases, ftp://ftp.wmo.int/Documents/PublicWeb/arep/gaw/gaw174.pdf, Tokyo.

Wunch, D., et al. (2010), Calibration of the Total Carbon Column Observing Network using aircraft profile data, *Atmos. Meas. Tech.*, *3*, 1351–1362, doi:10.5194/amt-3-1351-2010.

Wunch, D., et al. (2011a), The Total Carbon Column Observing Network, *Philos. Trans. R. Soc. A*, *369*, 2087–2112, doi:10.1098/rsta.2010.0240.

Wunch, D., et al. (2011b), A method for evaluating bias in global measurements of $CO_2$ total columns from space, *Atmos. Chem. Phys.*, *11*, 12,317–12,337, doi:10.5194/acp-11-12317-2011.

Yokota, T., Y. Yoshida, N. Eguchi, Y. Ota, T. Tanaka, H. Watanabe, and S. Maksyutov (2009), Global concentrations of $CO_2$ and $CH_4$ retrieved from GOSAT, first preliminary results, *Sci. Online Lett. Atmos.*, *5*, 160–163.

York, D., N. Evensen, M. Martínez, and J. Delgado (2004), Unified equations for the slope, intercept, and standard errors of the best straight line, *Am. J. Phys.*, *72*, 367–375, doi:10.1119/1.1632486.

Yoshida, Y., et al. (2011), Retrieval algorithm for $CO_2$ and $CH_4$ column abundances from short-wavelength infrared spectral observations by the Greenhouse Gases Observing Satellite, *Atmos. Meas. Tech.*, *4*, 717–734, doi:10.5194/amt-4-717-2011.